AIMS Mathematics, 11(11): 37837–37878.
DOI: 10.3934/math.20261463
Received: 10 August 2026
Revised: 26 September 2026
Accepted: 12 October 2026
Published: 13 November 2026

http://www.aimspress.com/journal/Math

Research article

Enhancing accuracy in time-fractional Schrödinger equation: a high-order B-spline collocation approach

Alaattin Esen[1,*], **Murat Önal**[1] **and Berat Karaagac**[2]

[1] Department of Mathematics, Faculty of Science and Arts, Inonu University, Malatya 44000, Turkey
[2] Department of Natural and Mathematical Sciences, Faculty of Engineering, Tarsus University, Mersin 33400, Turkey

* **Correspondence:** Email: alaattin.esen@inonu.edu.tr; Tel: +904223774288.

Abstract: The Schrödinger equation has an important place among the partial differential equations used in quantum mechanics, since it describes the time evolution of a physical system. In this paper, a numerical method is developed for the time-fractional nonlinear Schrödinger equation involving the Caputo fractional derivative. The temporal discretization is constructed using the L1 formula together with Crank–Nicolson-type averaging, and the nonlinear coefficient is evaluated explicitly at the previous time level. For the spatial discretization, a collocation method based on cubic B-splines is combined with a high-order approximation of the second spatial derivative. The resulting formulation leads to a linear algebraic system at each time step for the coefficients associated with the real and imaginary parts of the solution. A local consistency analysis is presented for sufficiently smooth solutions. The analysis shows that the complete discretization has local truncation error of order $O(\Delta t + h^4)$ so that the temporal discretization is first-order consistent, whereas the high-order spatial approximation is fourth-order accurate. These behaviors are also examined separately through temporal and spatial refinement studies. A nonsmooth test problem with a weak initial singularity is also considered to examine the numerical behavior of the method for a solution with limited temporal regularity. The numerical results exhibit approximately first-order temporal convergence for the smooth test problems and approximately fourth-order spatial convergence for Problem 1. Numerical experiments are further used to compare the performance of cubic, trigonometric, and uniform hyperbolic polynomial B-spline bases. A Fourier analysis of the corresponding linearized frozen-coefficient recurrence is also discussed. The numerical results and comparisons illustrate the accuracy of the proposed high-order B-spline collocation approach for the considered time-fractional Schrödinger problems.

Keywords: Schrödinger equation; collocation method; high-order approach; B-spline; Caputo fractional derivative; Fourier analysis

Mathematics Subject Classification: 65L60, 65M60, 42A15

1. Introduction

Fractional partial differential equations (FPDEs) have received considerable attention because of their ability to describe processes involving memory and nonlocal effects. In contrast to classical integer-order derivatives, fractional derivatives incorporate information from the previous history of the solution and therefore provide a useful mathematical framework for modeling systems whose present state depends on their past evolution. Applications of fractional differential equations arise in areas such as anomalous diffusion, viscoelasticity, transport and relaxation processes, and wave propagation in heterogeneous or complex media. Consequently, fractional models have been increasingly studied in physics, engineering, biology, and other applied sciences. Several definitions of fractional derivatives have been introduced, including the Riemann–Liouville, Caputo, and Caputo–Fabrizio derivatives. Among them, the Caputo derivative is particularly convenient for many initial-value problems because it permits the use of initial conditions expressed in terms of integer-order derivatives. The nonlocal character of the Caputo derivative, however, also introduces additional difficulties in the numerical approximation of fractional differential equations. In particular, the history dependence of the fractional derivative must be combined carefully with the discretization of the remaining spatial and nonlinear terms. Therefore, the construction and analysis of accurate numerical methods for fractional partial differential equations remain important computational problems. Among the equations considered in fractional form, the Schrödinger equation is of particular interest because of its fundamental role in quantum mechanics and wave propagation. In its classical form, the Schrödinger equation contains a first-order derivative in time and a second-order derivative in space [1]. Its nonlinear counterpart arises in several physical settings involving nonlinear wave phenomena, including nonlinear optics, surface water waves, and plasma physics [2]. Fractional generalizations of the Schrödinger equation have subsequently been considered in order to incorporate nonlocal effects into the mathematical model. Depending on the application, fractional operators may be introduced in the spatial variable, the temporal variable, or both.

In the present study, we consider the following time-fractional nonlinear Schrödinger equation involving the Caputo derivative:

$$i\,{}^{C}D_t^{\gamma}u(x,t) + u_{xx}(x,t) + |u(x,t)|^2u(x,t) = f(x,t), \qquad 0 < \gamma \le 1, \quad t \ge 0, \tag{1.1}$$

where $u(x,t)$ is a complex-valued function, i denotes the imaginary unit, $f(x,t)$ is a prescribed source term, and ${}^{C}D_t^{\gamma}$ denotes the Caputo fractional derivative of order γ with respect to time. The time-fractional formulation provides a mathematical framework in which temporal memory effects can be incorporated into the evolution of the wave function. A variety of analytical, semi-analytical, and numerical techniques have been developed for fractional Schrödinger-type and related nonlinear wave equations. Amer et al. [3] obtained exact optical soliton solutions for a fractional quadratic–cubic nonlinear Schrödinger equation involving a conformable derivative and also considered a numerical validation of their solutions. Mustafa and Murad [4] studied a time-fractional extended (3 + 1)-dimensional nonlinear Schrödinger equation with a conformable derivative, and they constructed

several classes of soliton solutions. Panwar et al. [5] investigated the time-fractional nonlinear Schrödinger and coupled Klein–Gordon–Schrödinger equations involving the Caputo derivative using a homotopy-analysis-based approach and discussed the convergence of the resulting approximation. Related semi-analytical studies have also contributed to the treatment of fractional nonlinear wave models. Hagag et al. [6] applied the q-homotopy analysis transform method to a fractional fourth-order dispersive cubic nonlinear Schrödinger equation, and Arafa and Hagag [7] employed the same general methodology for fractional Kundu–Eckhaus and massive Thirring models. More recent developments for related fractional nonlinear equations include neural-network-assisted exact-solution techniques for a conformable fractional Kolmogorov–Petrovskii–Piskunov model [8] and traveling-wave constructions for a paraxial wave equation involving a conformable fractional derivative [9]. Although these studies employ different fractional operators, equations, and solution strategies from those considered here, they illustrate the continuing development of analytical and semi-analytical techniques for fractional nonlinear wave problems. Numerical approaches based on collocation, finite differences, and finite elements have also been developed. Mohebbi et al. [10] employed a meshless collocation method based on radial basis functions for the time-fractional nonlinear Schrödinger equation. Hadhoud et al. [11] developed a trigonometric B-spline collocation method for the time-fractional Schrödinger equation. Bayrak and Demir [12] considered a fractional collocation technique for a space-fractional Schrödinger equation. Nemati et al. [13] employed fractional-order Chelyshkov functions for space–time fractional Schrödinger equations and transformed the separated real and imaginary equations into an algebraic system. Wang et al. [14] developed a modified L1 Crank–Nicolson finite element method for the nonlinear time-fractional Schrödinger equation and established stability and error estimates for its formulation. Zhou et al. [15] considered L1-2 finite element methods for nonlinear Schrödinger equations with a variable-order time-fractional derivative and analyzed the stability and convergence of their schemes. Serik et al. [16] constructed a high-accuracy finite-difference method for the time-fractional Schrödinger equation using an L1-type temporal approximation together with a fourth-order compact spatial discretization, and analyzed the corresponding stability and convergence properties. Hayat et al. [17] studied a cubic B-spline computational scheme for a fractional Schrödinger problem involving the Atangana–Baleanu derivative. These studies illustrate the variety of temporal and spatial discretizations that have been developed for fractional Schrödinger-type problems. B-spline collocation methods are particularly attractive for spatial discretization because of their local support, smoothness, and relatively simple algebraic structure. Nevertheless, the accuracy of the resulting method depends not only on the selected basis but also on the approximation used for the spatial derivatives. Related high-order B-spline constructions have also been considered for other time-fractional nonlinear equations. For example, Önal et al. [18] developed a higher-order trigonometric cubic B-spline collocation approach for time-fractional Burgers equations in which a high-order approximation of the second spatial derivative (as in the present work) was used. The present study differs from [18] in three respects. First, the equation considered here is a complex-valued nonlinear Schrödinger equation, which is treated as a coupled system for its real and imaginary parts. Second, cubic B-splines are used as the primary basis, and trigonometric and uniform hyperbolic polynomial B-splines are examined numerically. Third, the nonlinear term is frozen at the previous time level, so that each time step requires the solution of a linear system without nonlinear iteration, whereas [18] used the Rubin–Graves linearization. In addition, the present work provides a local consistency analysis and a Fourier resolvent analysis, whereas a

von Neumann stability analysis was used in [18]. In the present work, the main emphasis is placed on increasing the spatial accuracy of the collocation formulation by combining cubic B-splines with a high-order approximation of the second spatial derivative. The resulting construction retains the computational structure of B-spline collocation while providing a fourth-order spatial approximation for sufficiently smooth solutions. The temporal discretization requires separate consideration. The Caputo derivative is approximated using the L1 formula, whereas Crank–Nicolson-type averaging is employed for the spatial terms and the nonlinear coefficient is evaluated explicitly from the solution at the previous time level. Because these components do not all correspond to the same temporal location, the formal consistency order of the L1 approximation alone does not determine the temporal order of the complete scheme. Accordingly, a local consistency analysis is included to identify the contributions of the temporal and spatial discretizations. For sufficiently smooth solutions, the analysis gives the local discretization error

$$\mathcal{T} = O(\Delta t + h^4) \tag{1.2}$$

showing that the complete temporal treatment is first-order consistent, whereas the high-order spatial approximation retains fourth-order consistency. This distinction is also taken into account in the numerical assessment of the method. Temporal convergence is examined by refining Δt while keeping the spatial mesh fixed, whereas spatial convergence is examined by refining h with a fixed sufficiently small time step. Joint-refinement experiments are interpreted separately in accordance with (1.2). In particular, under the balanced refinement relation $\Delta t = Ch^4$, the temporal and spatial error contributions formally behave as

$$O(h^4) + O(h^4),$$

so that both contributions are of the same order and the observed rate in a joint-refinement experiment is expected to approach four, provided that the numerical errors follow the behavior suggested by the local consistency analysis. This distinction is important when interpreting convergence tables in which h and Δt are simultaneously refined. The numerical implementation is developed primarily using cubic B-spline basis functions. Trigonometric and uniform hyperbolic polynomial B-splines are also considered numerically in order to examine the influence of the basis family under comparable computational settings. These comparisons are treated as numerical investigations rather than as an assertion that the three basis families possess identical approximation or stability properties. Furthermore, a Fourier analysis is carried out for the corresponding linearized frozen-coefficient recurrence. The scope of this analysis is stated explicitly so that conclusions obtained for the linearized problem are not interpreted as a complete nonlinear stability result. The contribution of the present work is not the introduction of the L1 formula or B-spline collocation individually but rather their particular combination with the high-order spatial correction and, importantly, the explicit separation of the temporal and spatial error contributions. A local consistency analysis is provided to identify the effective temporal order of the complete discretization, and separate temporal and spatial refinement studies are used to examine the corresponding numerical behavior. This distinction also provides a consistent interpretation of joint-refinement experiments, for which the observed rate reflects both temporal and spatial errors rather than the spatial approximation alone. To the authors' knowledge, the combination of the L1 formula, B-spline collocation and the high-order spatial correction has not previously been considered for the time-fractional nonlinear Schrödinger equation. The remainder of the paper is organized as follows. In Section 2, the basic definitions used throughout the study are introduced, including the Caputo fractional derivative, the L1 discretization formula, and the B-spline basis functions. In Section 3,

the high-order approximation of the second spatial derivative is presented. Section 4 develops the fully discrete formulation for the time-fractional nonlinear Schrödinger equation and derives the resulting linear algebraic system. Section 5 then establishes the local consistency and truncation error of the complete discretization. Section 6 presents a Fourier analysis of the associated linearized frozen-coefficient recurrence. Finally, in Section 7, numerical experiments are used to investigate the temporal and spatial convergence behavior separately inorder to examine joint-refinement behavior, to investigate the numerical behavior of the method for a nonsmooth solution with a weak initial singularity, and to compare the numerical results with available reference results.

2. Preliminaries and definitions

In this section, the basic definitions and numerical ingredients required for the construction of the proposed method are introduced. We first recall the Caputo fractional derivative and its L1 approximation. We then present the B-spline collocation framework and the cubic, trigonometric cubic, and uniform hyperbolic polynomial B-spline basis functions considered in the numerical experiments.

2.1. The Caputo fractional derivative

The Caputo fractional derivative of order α of a sufficiently smooth function $x(t)$ is defined by

$$ {}^{C}D^{\alpha}_{0,t}x(t) = \frac{1}{\Gamma(m-\alpha)} \int_0^t (t-\tau)^{m-\alpha-1} x^{(m)}(\tau)\, d\tau, \qquad m-1 < \alpha < m, \quad m \in \mathbb{N}. \tag{2.1} $$

For a constant c, the Caputo derivative satisfies [19]

$$ {}^{C}D^{\alpha}_{0,t}c = 0. \tag{2.2} $$

Throughout this paper, the fractional derivative is understood in the Caputo sense, and its order is denoted by γ. Because the governing equation involves $0 < \gamma \leq 1$, for $0 < \gamma < 1$, we have $m = 1$ and

$$ {}^{C}D^{\gamma}_{t}x(t) = \frac{1}{\Gamma(1-\gamma)} \int_0^t (t-s)^{-\gamma} x'(s)\, ds. \tag{2.3} $$

The limiting case $\gamma = 1$ corresponds to the classical first-order time derivative.

2.2. The L1 discretization

Let

$$ 0 = t_0 < t_1 < \cdots < t_M = T, \qquad t_n = n\Delta t, \qquad \Delta t = \frac{T}{M}, \tag{2.4} $$

be a uniform temporal partition. For $0 < \gamma < 1$, the Caputo fractional derivative of a sufficiently smooth function $u(x,t)$ at $t = t_{n+1}$ is given by

$$ {}^{C}D^{\gamma}_{t}u(x,t_{n+1}) = \frac{1}{\Gamma(1-\gamma)} \int_0^{t_{n+1}} \frac{\partial u(x,s)/\partial s}{(t_{n+1}-s)^{\gamma}}\, ds. \tag{2.5} $$

Dividing the integration interval into the temporal subintervals $[t_k, t_{k+1}]$ gives

$$ {}^{C}D^{\gamma}_{t}u(x,t_{n+1}) = \frac{1}{\Gamma(1-\gamma)} \sum_{k=0}^{n} \int_{t_k}^{t_{k+1}} \frac{\partial u(x,s)/\partial s}{(t_{n+1}-s)^{\gamma}}\, ds. \tag{2.6} $$

On each interval $[t_k, t_{k+1}]$, the first derivative is approximated by

$$\frac{\partial u(x,s)}{\partial s} = \frac{u(x,t_{k+1}) - u(x,t_k)}{\Delta t} + O(\Delta t), \qquad s \in [t_k, t_{k+1}]. \tag{2.7}$$

Substituting this approximation into (2.6) and evaluating the kernel integral exactly leads to the standard L1 approximation

$${}^{C}D_t^{\gamma} u(x,t_{n+1}) = \frac{(\Delta t)^{-\gamma}}{\Gamma(2-\gamma)} \sum_{k=0}^{n} b_k \left[u(x,t_{n+1-k}) - u(x,t_{n-k})\right] + r_{\Delta t}^{n+1}, \tag{2.8}$$

where

$$b_k = (k+1)^{1-\gamma} - k^{1-\gamma}, \qquad k = 0, 1, 2, \ldots. \tag{2.9}$$

For sufficiently smooth u, the local truncation error of the $L1$ approximation satisfies

$$r_{\Delta t}^{n+1} = O\Big((\Delta t)^{2-\gamma}\Big), \qquad 0 < \gamma < 1; \tag{2.10}$$

see [20]. For later use, we introduce the discrete L1 operator

$$D_{\Delta t}^{\gamma} u^{n+1} = \frac{(\Delta t)^{-\gamma}}{\Gamma(2-\gamma)} \sum_{k=0}^{n} b_k \left(u^{n-k+1} - u^{n-k}\right). \tag{2.11}$$

Thus,

$${}^{C}D_t^{\gamma} u(t_{n+1}) = D_{\Delta t}^{\gamma} u^{n+1} + O\Big((\Delta t)^{2-\gamma}\Big). \tag{2.12}$$

It should be emphasized that (2.12) describes the consistency order of the L1 approximation itself. It does not by itself determine the temporal consistency order of the complete numerical scheme, as the remaining terms of the governing equation are treated at different temporal levels. The consistency of the fully discrete method is therefore examined separately in the subsequent analysis.

Lemma 2.1. *Let* $0 < \gamma < 1$ *and*

$$b_k = (k+1)^{1-\gamma} - k^{1-\gamma}, \qquad k = 0, 1, 2, \ldots.$$

Then

$$1 = b_0 > b_1 > b_2 > \cdots > 0, \qquad b_k \to 0 \quad \text{as} \quad k \to \infty.$$

Remark 2.2. The properties stated in Lemma 2.1 follow from the monotonicity and concavity of $x^{1-\gamma}$ for $0 < \gamma < 1$. They are also established in [21] in the more general setting of a variable fractional order. The constant-order case considered here is obtained as a particular case.

2.3. B-spline collocation

Spline functions are piecewise-defined functions satisfying prescribed continuity conditions at the knots. B-splines provide locally supported basis functions and are therefore convenient for the construction of collocation approximations [22]. In what follows, a B-spline is a spline function of minimal support, the functions ϕ_j are the B-spline basis functions obtained by translation on the

uniform knot sequence, and a B-spline family is the cubic; the trigonometric cubic or the uniform hyperbolic polynomial type.

Let the spatial interval $[a, b]$ be divided uniformly as

$$a = x_0 < x_1 < \cdots < x_N = b, \qquad h = x_{m+1} - x_m = \frac{b-a}{N}. \tag{2.13}$$

The knot sequence is extended outside the physical interval where necessary so that the B-spline basis functions are well–defined near the boundaries. For a sufficiently smooth function $u(x, t)$, its B-spline collocation approximation is represented by

$$u(x,t) \approx U_h(x,t) = \sum_{j=-1}^{N+1} \delta_j(t)\phi_j(x), \tag{2.14}$$

where $\phi_j(x)$ denotes the selected B-spline basis function and $\delta_j(t)$ are time-dependent coefficients. The coefficients are determined from the collocation equations together with the prescribed boundary conditions [23]. For the B-spline families considered below, the nodal values of the approximation and its second spatial derivative can be expressed in the common algebraic form

$$U_h(x_m,t) = a_1\delta_{m-1}(t) + a_2\delta_m(t) + a_3\delta_{m+1}(t), \tag{2.15}$$

$$(U_h)_x(x_m,t) = d_1\delta_{m-1}(t) + d_2\delta_{m+1}(t), \tag{2.16}$$

$$(U_h)_{xx}(x_m,t) = c_1\delta_{m-1}(t) + c_2\delta_m(t) + c_3\delta_{m+1}(t). \tag{2.17}$$

The coefficients a_i, d_i, and c_i depend on the particular B-spline family and on the spatial mesh size. The representation (2.15)–(2.17) is used as a common algebraic framework for assembling the collocation equations. This common representation should not be interpreted as implying identical approximation, consistency, or stability properties for the different basis families. The higher-order spatial analysis developed in the present work is associated with the corrected cubic B-spline construction, whereas the trigonometric and uniform hyperbolic polynomial B-spline bases are also considered for numerical comparison.

2.3.1. Cubic B-splines

The cubic B-spline basis function associated with the node x_m is defined by

$$B_{m,3}(x) = \frac{1}{h^3}\begin{cases} (x - x_{m-2})^3, & x \in [x_{m-2}, x_{m-1}), \\ (x - x_{m-2})^3 - 4(x - x_{m-1})^3, & x \in [x_{m-1}, x_m), \\ (x_{m+2} - x)^3 - 4(x_{m+1} - x)^3, & x \in [x_m, x_{m+1}), \\ (x_{m+2} - x)^3, & x \in [x_{m+1}, x_{m+2}), \\ 0, & \text{otherwise.} \end{cases} \tag{2.18}$$

Thus, $B_{m,3}(x)$ has compact support on $[x_{m-2}, x_{m+2}]$. With the normalization used in (2.18), the coefficients in (2.15)–(2.17) are

$$a_1 = a_3 = 1, \qquad a_2 = 4; \tag{2.19}$$

$$d_1 = -\frac{3}{h}, \qquad d_2 = \frac{3}{h}; \tag{2.20}$$

and

$$c_1 = c_3 = \frac{6}{h^2}, \qquad c_2 = -\frac{12}{h^2}. \tag{2.21}$$

2.3.2. Trigonometric cubic B-splines

For comparison purposes, trigonometric cubic B-splines are also considered. These basis functions are constructed from trigonometric functions and have compact support on the corresponding knot intervals [24]. Define

$$p_j(x) = \sin\left(\frac{x - x_j}{2}\right) \tag{2.22}$$

and

$$\vartheta = \sin\left(\frac{h}{2}\right)\sin(h)\sin\left(\frac{3h}{2}\right). \tag{2.23}$$

The trigonometric cubic B-spline associated with the knot x_j is

$$T_{3,j}(x) = \frac{1}{\vartheta}\begin{cases} p_j^3(x), & x_j < x < x_{j+1}, \\ -p_j^2(x)p_{j+2}(x) - p_j(x)p_{j+3}(x)p_{j+1}(x) - p_{j+4}(x)p_{j+1}^2(x), & x_{j+1} < x < x_{j+2}, \\ p_j(x)p_{j+3}^2(x) + p_{j+4}(x)p_{j+3}(x)p_{j+1}(x) + p_{j+4}^2(x)p_{j+2}(x), & x_{j+2} < x < x_{j+3}, \\ -p_{j+4}^3(x), & x_{j+3} < x < x_{j+4}, \\ 0, & \text{otherwise.} \end{cases} \tag{2.24}$$

The corresponding coefficients in (2.15)–(2.17) are

$$a_1 = a_3 = \sin^2\left(\frac{h}{2}\right)\csc(h)\csc\left(\frac{3h}{2}\right), \tag{2.25}$$

$$a_2 = \frac{2}{1 + 2\cos h}, \tag{2.26}$$

$$d_1 = -\frac{3}{4}\csc\left(\frac{3h}{2}\right), \qquad d_2 = \frac{3}{4}\csc\left(\frac{3h}{2}\right), \tag{2.27}$$

$$c_1 = c_3 = \frac{3\left(3\cos^2\left(\frac{h}{2}\right) - 1\right)}{4\sin(h)\sin\left(\frac{3h}{2}\right)}, \tag{2.28}$$

$$c_2 = -\frac{3\cot^2\left(\frac{h}{2}\right)}{2 + 4\cos h}. \tag{2.29}$$

These coefficients provide the nodal collocation relations for the trigonometric basis. Their use in the numerical experiments does not imply that the approximation or stability properties established for the cubic B-spline construction automatically extend to the trigonometric basis.

2.3.3. Uniform hyperbolic polynomial B-splines

Uniform hyperbolic polynomial B-splines are also considered as an alternative basis in the numerical comparisons [25]. Because the spatial mesh is uniform, the notation Δx used in some definitions of this basis is identified here with the mesh size h. Define

$$p_1 = 2h(\cosh h - 1). \tag{2.30}$$

The fourth-order uniform hyperbolic polynomial B-spline associated with x_i is given by

$$H_i^4(x) = \frac{1}{p_1}\begin{cases} \sinh(x - x_{i-2}) - (x - x_{i-2}), & x_{i-2} \le x \le x_{i-1}, \\ -2\sinh(x - x_{i-1}) - \sinh(x - x_i) + (2\cosh h + 1)(x - x_i) + 2h\cosh h, & x_{i-1} \le x \le x_i, \\ \sinh(x - x_i) + 2\sinh(x - x_{i+1}) - (2\cosh h + 1)(x - x_i) + 2h\cosh h, & x_i \le x \le x_{i+1}, \\ -\sinh(x - x_{i+2}) + (x - x_{i+2}), & x_{i+1} \le x \le x_{i+2}, \\ 0, & \text{otherwise.} \end{cases} \tag{2.31}$$

The corresponding nodal coefficients in (2.15)–(2.17) are

$$a_1 = a_3 = \frac{\sinh h - h}{p_1}, \tag{2.32}$$

$$a_2 = -\frac{2(\sinh h - h\cosh h)}{p_1}, \tag{2.33}$$

$$d_1 = -\frac{1}{2h}, \qquad d_2 = \frac{1}{2h}, \tag{2.34}$$

$$c_1 = c_3 = \frac{\sinh h}{p_1}, \tag{2.35}$$

$$c_2 = -\frac{2\sinh h}{p_1}. \tag{2.36}$$

The relations above provide the nodal algebraic representation required for the numerical implementation of the uniform hyperbolic polynomial basis. As in the trigonometric case, no assumption is made that the consistency or stability properties established for the corrected cubic B-spline discretization transfer automatically to this basis without a separate analysis.

3. High-order approximation of the second spatial derivative

We now present a higher-order approximation of the solution and its derivatives at the nodes. Let $I_h u(x,t)$ denote the cubic spline interpolant of $u(x,t)$ on the uniform grid. At the collocation nodes x_j, it satisfies the interpolation and boundary conditions

$$\begin{aligned} (I_h u)(x_j,t) &= u(x_j,t), \qquad 0 \le j \le N, \\ (I_h u)''(x_j,t) &= u''(x_j,t) - \frac{1}{12}h^2 u^{(4)}(x_j,t), \qquad j = 0, N. \end{aligned} \tag{3.1}$$

If $u(x,t)$ is of class C^6 on $[a,b]$ in x and $I_h u(x,t)$ satisfies these conditions, then

$$(I_h u)''(x_j,t) = u''(x_j,t) - \frac{1}{12}h^2 u^{(4)}(x_j,t) + O(h^4), \qquad 0 \le j \le N. \tag{3.2}$$

This is Eq (1.3) of [26]; the bound follows from two lemmas of that paper. Put

$$e_j = u''(x_j,t) - \frac{h^2}{12}u^{(4)}(x_j,t) - (I_h u)''(x_j,t).$$

By [26, Lemma 2], for a uniform mesh,

$$e_{j-1} + 4e_j + e_{j+1} = \eta_j, \qquad 1 \le j \le N-1, \qquad |\eta_j| \le Kh^4 \,\|u^{(6)}\|_\infty,$$

and the end conditions in (3.1) give $e_0 = e_N = 0$. The matrix tridiag$(1,4,1)$ is strictly diagonally dominant, so [26, Lemma 4] gives $\max_j |e_j| \le \max_j |\eta_j|/2$, and (3.2) follows. To eliminate the term $u^{(4)}$ from (3.2), it is approximated by finite differences. At the interior nodes, a central difference of the second derivative gives

$$u^{(4)}(x_j,t) = \frac{(I_h u)''(x_{j-1},t) - 2(I_h u)''(x_j,t) + (I_h u)''(x_{j+1},t)}{h^2} + O(h^2), \qquad 1 \le j \le N-1. \tag{3.3}$$

Because this formula cannot be applied at the two end nodes, the values there are obtained by linear extrapolation:

$$u^{(4)}(x_0,t) = 2u^{(4)}(x_1,t) - u^{(4)}(x_2,t), \qquad u^{(4)}(x_N,t) = 2u^{(4)}(x_{N-1},t) - u^{(4)}(x_{N-2},t), \tag{3.4}$$

which, after substituting (3.3), yields one-sided formulas at x_0 and x_N. Collecting all three cases, the fourth derivative is approximated by

$$\begin{aligned}
u^{(4)}(x_j,t) &= \frac{2(I_h u)''(x_0,t) - 5(I_h u)''(x_1,t) + 4(I_h u)''(x_2,t) - (I_h u)''(x_3,t)}{h^2} + O(h^2), \qquad j = 0, \qquad (3.5)\\
u^{(4)}(x_j,t) &= \frac{(I_h u)''(x_{j-1},t) - 2(I_h u)''(x_j,t) + (I_h u)''(x_{j+1},t)}{h^2} + O(h^2), \qquad 1 \le j \le N-1,\\
u^{(4)}(x_j,t) &= \frac{2(I_h u)''(x_N,t) - 5(I_h u)''(x_{N-1},t) + 4(I_h u)''(x_{N-2},t) - (I_h u)''(x_{N-3},t)}{h^2} + O(h^2), \qquad j = N.
\end{aligned}$$

Substituting these expressions into (3.2) removes the $u^{(4)}$ term and gives the high-order approximation of the second derivative [27, 28]

$$\begin{aligned}
u''(x_0,t) &= \frac{14(I_h u)''(x_0,t) - 5(I_h u)''(x_1,t) + 4(I_h u)''(x_2,t) - (I_h u)''(x_3,t)}{12} + O(h^4), \qquad j = 0, \qquad (3.6)\\
u''(x_j,t) &= \frac{(I_h u)''(x_{j-1},t) + 10(I_h u)''(x_j,t) + (I_h u)''(x_{j+1},t)}{12} + O(h^4), \qquad 1 \le j \le N-1,\\
u''(x_N,t) &= \frac{-(I_h u)''(x_{N-3},t) + 4(I_h u)''(x_{N-2},t) - 5(I_h u)''(x_{N-1},t) + 14(I_h u)''(x_N,t)}{12} + O(h^4), \qquad j = N.
\end{aligned}$$

The formulas (3.6) are those of [26, Theorem 1, (vi), (viii), (viii)′]; for $u \in C^6$ and the end conditions (3.1) they hold with error $O(h^4)$. For later reference, we denote by $\mathcal{D}^{(4)}_{h,j}u(x_j,t)$ the right-hand side of (3.6) without the $O(h^4)$ term; that is,

$$\mathcal{D}^{(4)}_{h,j}u(x_j,t) = \frac{1}{12}\Big[(I_h u)''(x_{j-1},t) + 10(I_h u)''(x_j,t) + (I_h u)''(x_{j+1},t)\Big], \qquad 1 \le j \le N-1,$$

with the corresponding one-sided expressions for $j = 0$ and $j = N$. Thus $u''(x_j,t) = \mathcal{D}^{(4)}_{h,j}u(x_j,t) + O(h^4)$ for $0 \le j \le N$.

4. The fully discrete scheme for the time-fractional nonlinear Schrödinger equation

As discussed in the previous sections, finding numerical solutions of the time-fractional Schrödinger equation is of considerable importance. In this section, a numerical scheme is constructed for the following fractional-order Schrödinger equation:

$$i\,{}^{C}D_t^{\gamma}u + \frac{\partial^2 u}{\partial x^2} + |u|^2 u = f(x,t), \qquad 0 < \gamma \le 1, \quad t \ge 0, \tag{4.1}$$

together with the boundary conditions

$$u(a,t) = u_a(t), \qquad u(b,t) = u_b(t), \qquad t \ge 0, \tag{4.2}$$

and the initial condition

$$u(x,0) = u_0(x). \tag{4.3}$$

Because $u(x,t)$ is a complex-valued function, it can be decomposed as

$$u(x,t) = R(x,t) + iS(x,t), \tag{4.4}$$

where $R(x,t)$ and $S(x,t)$ denote the real and imaginary parts, respectively. Writing $u = R + iS$, the fractional time derivative takes the form

$$i\,{}^{C}D_t^{\gamma}u = i\,{}^{C}D_t^{\gamma}R - {}^{C}D_t^{\gamma}S. \tag{4.5}$$

Similarly, the spatial and nonlinear terms become

$$u_{xx} = R_{xx} + iS_{xx}, \qquad |u|^2 u = (R^2 + S^2)(R + iS). \tag{4.6}$$

When these expressions are substituted into Eq (4.1) and the real and imaginary parts are separated, the following coupled system appears:

$${}^{C}D_t^{\gamma}S - R_{xx} - (R^2 + S^2)R = -f_r(x,t), \tag{4.7}$$

$${}^{C}D_t^{\gamma}R + S_{xx} + (R^2 + S^2)S = f_s(x,t), \tag{4.8}$$

where

$$f(x,t) = f_r(x,t) + if_s(x,t).$$

At the collocation points, the approximate solutions for R and S are expressed in terms of the selected B-spline basis functions as

$$\begin{aligned} R_j^n &= a_1\delta_{j-1}^n + a_2\delta_j^n + a_3\delta_{j+1}^n, \\ (R_{xx})_j^n &= c_1\delta_{j-1}^n + c_2\delta_j^n + c_3\delta_{j+1}^n, \end{aligned} \tag{4.9}$$

and

$$\begin{aligned} S_j^n &= a_1\sigma_{j-1}^n + a_2\sigma_j^n + a_3\sigma_{j+1}^n, \\ (S_{xx})_j^n &= c_1\sigma_{j-1}^n + c_2\sigma_j^n + c_3\sigma_{j+1}^n. \end{aligned} \tag{4.10}$$

For convenience, the nonlinear coefficient is denoted by

$$Z_j^n = (R_j^n)^2 + (S_j^n)^2, \tag{4.11}$$

evaluated explicitly at the known time level t_n and held fixed while computing the solution at t_{n+1}. This treatment keeps the algebraic system linear with respect to the unknown coefficients at t_{n+1}. Equations (4.7) and (4.8) may therefore be written in the compact form

$${}^{C}D_t^{\gamma} S - R_{xx} - ZR = -f_r, \tag{4.12}$$

$${}^{C}D_t^{\gamma} R + S_{xx} + ZS = f_s. \tag{4.13}$$

The Caputo fractional derivative is now approximated by the L1 formula, and a Crank–Nicolson-type averaging is applied to the remaining terms. The nonlinear coefficient is evaluated at the known time level t_n. Thus, Eqs (4.12) and (4.13) become

$$\frac{\Delta t^{-\gamma}}{\Gamma(2-\gamma)} \sum_{k=0}^{n} b_k \left[S_j^{n-k+1} - S_j^{n-k} \right] - \frac{(R_{xx})_j^{n+1} + (R_{xx})_j^n}{2} - Z_j^n \frac{R_j^{n+1} + R_j^n}{2} = -f_r(x_j, t_{n+\frac{1}{2}}) \tag{4.14}$$

and

$$\frac{\Delta t^{-\gamma}}{\Gamma(2-\gamma)} \sum_{k=0}^{n} b_k \left[R_j^{n-k+1} - R_j^{n-k} \right] + \frac{(S_{xx})_j^{n+1} + (S_{xx})_j^n}{2} + Z_j^n \frac{S_j^{n+1} + S_j^n}{2} = f_s(x_j, t_{n+\frac{1}{2}}), \tag{4.15}$$

where

$$t_{n+\frac{1}{2}} = \frac{t_n + t_{n+1}}{2}.$$

Denoting $s = \Delta t^{\gamma}\Gamma(2-\gamma)$ and rearranging the terms, these equations can be written as

$$S_j^{n+1} - \frac{s}{2}(R_{xx})_j^{n+1} - Z_j^n \frac{s}{2} R_j^{n+1} = S_j^n + \frac{s}{2}(R_{xx})_j^n + Z_j^n \frac{s}{2} R_j^n - s\, f_r(x_j, t_{n+\frac{1}{2}}) - \sum_{k=1}^{n} b_k \left[S_j^{n-k+1} - S_j^{n-k} \right], \tag{4.16}$$

$$R_j^{n+1} + \frac{s}{2}(S_{xx})_j^{n+1} + Z_j^n \frac{s}{2} S_j^{n+1} = R_j^n - \frac{s}{2}(S_{xx})_j^n - Z_j^n \frac{s}{2} S_j^n + s\, f_s(x_j, t_{n+\frac{1}{2}}) - \sum_{k=1}^{n} b_k \left[R_j^{n-k+1} - R_j^{n-k} \right]. \tag{4.17}$$

Substituting the B-spline approximations (4.9)-(4.10) together with the high-order formulas of Section 3 into Eqs (4.16)-(4.17) and after some arrangements, we have

$$
j=0 \Rightarrow \begin{cases} a_1\sigma_{-1}^{n+1}+a_2\sigma_0^{n+1}+a_3\sigma_1^{n+1}+\delta_{-1}^{n+1}\left[-\frac{s}{24}(14c_1)-Z_0^n\frac{s}{2}a_1\right]+\delta_0^{n+1}\left[-\frac{s}{24}(14c_2-5c_1)-Z_0^n\frac{s}{2}a_2\right] \\ +\delta_1^{n+1}\left[-\frac{s}{24}(14c_3-5c_2+4c_1)-Z_0^n\frac{s}{2}a_3\right]+\delta_2^{n+1}\left[-\frac{s}{24}(-5c_3+4c_2-c_1)\right] \\ +\delta_3^{n+1}\left[-\frac{s}{24}(4c_3-c_2)\right]+\delta_4^{n+1}\left[-\frac{s}{24}(-c_3)\right] \\ =a_1\sigma_{-1}^{n}+a_2\sigma_0^{n}+a_3\sigma_1^{n}+\delta_{-1}^{n}\left[\frac{s}{24}(14c_1)+Z_0^n\frac{s}{2}a_1\right]+\delta_0^{n}\left[\frac{s}{24}(14c_2-5c_1)+Z_0^n\frac{s}{2}a_2\right] \\ +\delta_1^{n}\left[\frac{s}{24}(14c_3-5c_2+4c_1)+Z_0^n\frac{s}{2}a_3\right]+\delta_2^{n}\left[\frac{s}{24}(-5c_3+4c_2-c_1)\right] \\ +\delta_3^{n}\left[\frac{s}{24}(4c_3-c_2)\right]+\delta_4^{n}\left[\frac{s}{24}(-c_3)\right]-s\,f_r(x_0,t_{n+\frac{1}{2}})-\sum_{k=1}^{n}b_k\left[S_0^{n-k+1}-S_0^{n-k}\right]. \end{cases} \tag{4.18}
$$

For the interior points $j=1,2,\ldots,N-1$, the same substitution and arrangements lead to

$$
j=1,2,\ldots,N-1 \Rightarrow \begin{cases} a_1\sigma_{j-1}^{n+1}+a_2\sigma_j^{n+1}+a_3\sigma_{j+1}^{n+1}+\delta_{j-2}^{n+1}\left[-\frac{s}{24}(c_1)\right]+\delta_{j-1}^{n+1}\left[-\frac{s}{24}(c_2+10c_1)-Z_j^n\frac{s}{2}a_1\right] \\ +\delta_j^{n+1}\left[-\frac{s}{24}(c_3+10c_2+c_1)-Z_j^n\frac{s}{2}a_2\right]+\delta_{j+1}^{n+1}\left[-\frac{s}{24}(10c_3+c_2)-Z_j^n\frac{s}{2}a_3\right] \\ +\delta_{j+2}^{n+1}\left[-\frac{s}{24}(c_3)\right] \\ =a_1\sigma_{j-1}^{n}+a_2\sigma_j^{n}+a_3\sigma_{j+1}^{n}+\delta_{j-2}^{n}\left[\frac{s}{24}(c_1)\right]+\delta_{j-1}^{n}\left[\frac{s}{24}(c_2+10c_1)+Z_j^n\frac{s}{2}a_1\right] \\ +\delta_j^{n}\left[\frac{s}{24}(c_3+10c_2+c_1)+Z_j^n\frac{s}{2}a_2\right]+\delta_{j+1}^{n}\left[\frac{s}{24}(10c_3+c_2)+Z_j^n\frac{s}{2}a_3\right] \\ +\delta_{j+2}^{n}\left[\frac{s}{24}(c_3)\right]-s\,f_r(x_j,t_{n+\frac{1}{2}})-\sum_{k=1}^{n}b_k\left[S_j^{n-k+1}-S_j^{n-k}\right]. \end{cases}
$$

Finally, for the right boundary $j=N$,

$$
j=N \Rightarrow \begin{cases} a_1\sigma_{N-1}^{n+1}+a_2\sigma_N^{n+1}+a_3\sigma_{N+1}^{n+1}+\delta_{N-4}^{n+1}\left[-\frac{s}{24}(-c_1)\right]+\delta_{N-3}^{n+1}\left[-\frac{s}{24}(-c_2+4c_1)\right] \\ +\delta_{N-2}^{n+1}\left[-\frac{s}{24}(-c_3+4c_2-5c_1)\right] \\ +\delta_{N-1}^{n+1}\left[-\frac{s}{24}(4c_3-5c_2+14c_1)-Z_N^n\frac{s}{2}a_1\right]+\delta_N^{n+1}\left[-\frac{s}{24}(-5c_3+14c_2)-Z_N^n\frac{s}{2}a_2\right] \\ +\delta_{N+1}^{n+1}\left[-\frac{s}{24}(14c_3)-Z_N^n\frac{s}{2}a_3\right] \\ =a_1\sigma_{N-1}^{n}+a_2\sigma_N^{n}+a_3\sigma_{N+1}^{n}+\delta_{N-4}^{n}\left[\frac{s}{24}(-c_1)\right]+\delta_{N-3}^{n}\left[\frac{s}{24}(-c_2+4c_1)\right] \\ +\delta_{N-2}^{n}\left[\frac{s}{24}(-c_3+4c_2-5c_1)\right]+\delta_{N-1}^{n}\left[\frac{s}{24}(4c_3-5c_2+14c_1)+Z_N^n\frac{s}{2}a_1\right] \\ +\delta_N^{n}\left[\frac{s}{24}(-5c_3+14c_2)+Z_N^n\frac{s}{2}a_2\right]+\delta_{N+1}^{n}\left[\frac{s}{24}(14c_3)+Z_N^n\frac{s}{2}a_3\right] \\ -s\,f_r(x_N,t_{n+\frac{1}{2}})-\sum_{k=1}^{n}b_k\left[S_N^{n-k+1}-S_N^{n-k}\right]. \end{cases}
$$

The same procedure is repeated for Eq (4.17). Substituting the approximations (4.9)-(4.10) together with the high-order formulas into (4.17) produces the following:

$$
j=0 \Rightarrow \begin{cases} a_1\delta_{-1}^{n+1}+a_2\delta_0^{n+1}+a_3\delta_1^{n+1}+\sigma_{-1}^{n+1}\left[\frac{s}{24}(14c_1)+Z_0^n\frac{s}{2}a_1\right]+\sigma_0^{n+1}\left[\frac{s}{24}(14c_2-5c_1)+Z_0^n\frac{s}{2}a_2\right] \\ +\sigma_1^{n+1}\left[\frac{s}{24}(14c_3-5c_2+4c_1)+Z_0^n\frac{s}{2}a_3\right]+\sigma_2^{n+1}\left[\frac{s}{24}(-5c_3+4c_2-c_1)\right] \\ +\sigma_3^{n+1}\left[\frac{s}{24}(4c_3-c_2)\right]+\sigma_4^{n+1}\left[\frac{s}{24}(-c_3)\right] \\ =a_1\delta_{-1}^{n}+a_2\delta_0^{n}+a_3\delta_1^{n}+\sigma_{-1}^{n}\left[-\frac{s}{24}(14c_1)-Z_0^n\frac{s}{2}a_1\right]+\sigma_0^{n}\left[-\frac{s}{24}(14c_2-5c_1)-Z_0^n\frac{s}{2}a_2\right] \\ +\sigma_1^{n}\left[-\frac{s}{24}(14c_3-5c_2+4c_1)-Z_0^n\frac{s}{2}a_3\right]+\sigma_2^{n}\left[-\frac{s}{24}(-5c_3+4c_2-c_1)\right]+\sigma_3^{n}\left[-\frac{s}{24}(4c_3-c_2)\right] \\ +\sigma_4^{n}\left[-\frac{s}{24}(-c_3)\right]+s\,f_s(x_0,t_{n+\frac{1}{2}})-\sum_{k=1}^{n}b_k\left[R_0^{n-k+1}-R_0^{n-k}\right]. \end{cases}
$$

In the same way,

$$j = 1, 2, \ldots, N-1 \Rightarrow \begin{cases} a_1\delta_{j-1}^{n+1} + a_2\delta_j^{n+1} + a_3\delta_{j+1}^{n+1} + \sigma_{j-2}^{n+1}\left[\frac{s}{24}(c_1)\right] + \sigma_{j-1}^{n+1}\left[\frac{s}{24}(c_2 + 10c_1) + Z_j^n\frac{s}{2}a_1\right] \\ +\sigma_j^{n+1}\left[\frac{s}{24}(c_3 + 10c_2 + c_1) + Z_j^n\frac{s}{2}a_2\right] + \sigma_{j+1}^{n+1}\left[\frac{s}{24}(10c_3 + c_2) + Z_j^n\frac{s}{2}a_3\right] \\ +\sigma_{j+2}^{n+1}\left[\frac{s}{24}(c_3)\right] \\ = a_1\delta_{j-1}^n + a_2\delta_j^n + a_3\delta_{j+1}^n + \sigma_{j-2}^n\left[-\frac{s}{24}(c_1)\right] + \sigma_{j-1}^n\left[-\frac{s}{24}(c_2 + 10c_1) - Z_j^n\frac{s}{2}a_1\right] \\ +\sigma_j^n\left[-\frac{s}{24}(c_3 + 10c_2 + c_1) - Z_j^n\frac{s}{2}a_2\right] + \sigma_{j+1}^n\left[-\frac{s}{24}(10c_3 + c_2) - Z_j^n\frac{s}{2}a_3\right] \\ +\sigma_{j+2}^n\left[-\frac{s}{24}(c_3)\right] + s\,f_s(x_j, t_{n+\frac{1}{2}}) - \sum_{k=1}^n b_k\left[R_j^{n-k+1} - R_j^{n-k}\right], \end{cases}$$

and

$$j = N \Rightarrow \begin{cases} a_1\delta_{N-1}^{n+1} + a_2\delta_N^{n+1} + a_3\delta_{N+1}^{n+1} + \sigma_{N-4}^{n+1}\left[\frac{s}{24}(-c_1)\right] + \sigma_{N-3}^{n+1}\left[\frac{s}{24}(-c_2 + 4c_1)\right] \\ +\sigma_{N-2}^{n+1}\left[\frac{s}{24}(-c_3 + 4c_2 - 5c_1)\right] + \sigma_{N-1}^{n+1}\left[\frac{s}{24}(4c_3 - 5c_2 + 14c_1) + Z_N^n\frac{s}{2}a_1\right] \\ +\sigma_N^{n+1}\left[\frac{s}{24}(-5c_3 + 14c_2) + Z_N^n\frac{s}{2}a_2\right] + \sigma_{N+1}^{n+1}\left[\frac{s}{24}(14c_3) + Z_N^n\frac{s}{2}a_3\right] \\ = a_1\delta_{N-1}^n + a_2\delta_N^n + a_3\delta_{N+1}^n + \sigma_{N-4}^n\left[-\frac{s}{24}(-c_1)\right] + \sigma_{N-3}^n\left[-\frac{s}{24}(-c_2 + 4c_1)\right] \\ +\sigma_{N-2}^n\left[-\frac{s}{24}(-c_3 + 4c_2 - 5c_1)\right] + \sigma_{N-1}^n\left[-\frac{s}{24}(4c_3 - 5c_2 + 14c_1) - Z_N^n\frac{s}{2}a_1\right] \\ +\sigma_N^n\left[-\frac{s}{24}(-5c_3 + 14c_2) - Z_N^n\frac{s}{2}a_2\right] + \sigma_{N+1}^n\left[-\frac{s}{24}(14c_3) - Z_N^n\frac{s}{2}a_3\right] \\ +s\,f_s(x_N, t_{n+\frac{1}{2}}) - \sum_{k=1}^n b_k\left[R_N^{n-k+1} - R_N^{n-k}\right]. \end{cases}$$

The system obtained above contains $2N + 2$ equations and $2N + 6$ unknowns. The extra unknowns δ_{-1}, δ_{N+1}, σ_{-1}, and σ_{N+1} are eliminated by using the boundary values of the approximation functions, which reduces the system to $(2N + 2) \times (2N + 2)$. Notice that no nonlinear iteration is required at this stage, because the nonlinear coefficient Z_j^n is already known from the previous time level. Before the time stepping can begin, the initial coefficients need to be determined. Using the boundary conditions $u(a, t)$ and $u(b, t)$, we obtain the following systems for the real and imaginary parts, respectively:

$$\begin{aligned} &(a_1\delta_{-1} + a_2\delta_0 + a_3\delta_1)^0 = R(x_0, 0) \\ &(a_1\delta_0 + a_2\delta_1 + a_3\delta_2)^0 = R(x_1, 0) \\ &\vdots \\ &(a_1\delta_{N-1} + a_2\delta_N + a_3\delta_{N+1})^0 = R(x_N, 0) \end{aligned}$$

and

$$\begin{aligned} &(a_1\sigma_{-1} + a_2\sigma_0 + a_3\sigma_1)^0 = S(x_0, 0) \\ &(a_1\sigma_0 + a_2\sigma_1 + a_3\sigma_2)^0 = S(x_1, 0) \\ &\vdots \\ &(a_1\sigma_{N-1} + a_2\sigma_N + a_3\sigma_{N+1})^0 = S(x_N, 0). \end{aligned}$$

It should be noted that the elimination procedure used at the initial time differs from that employed in the time-stepping scheme. At t_{n+1}, the prescribed Dirichlet boundary values constitute information independent of the discretized PDE residual equations above, and can therefore be used directly to eliminate the exterior coefficients. At $t = 0$, however, the nodal equations above already enforce the initial data $u_0(x)$ at every collocation point, including the boundary nodes; consequently, the boundary value alone does not provide an independent relation at this level. The second-derivative conditions below, which follow from the known smoothness of the initial data, supply the additional independent information required to close the initial systems. Now, as with the main numerical scheme, we have

$(2N+2)$ equations and $(2N+6)$ unknowns. Thus, δ^0_{-1}, δ^0_{N+1}, σ^0_{-1}, and σ^0_{N+1} need to be eliminated using the boundary values of $R''_j(x,t)$ and $S''_j(x,t)$, to obtain two systems, each in the form of $(N+1)$ equations with $(N+1)$ unknowns, as follows

$$\begin{aligned}
&\left(a_2 - a_1\tfrac{c_2}{c_1}\right)\delta^0_0 + \left(a_3 - a_1\tfrac{c_3}{c_1}\right)\delta^0_1 = R(x_0,0) - \tfrac{a_1}{c_1}R''(x_0,0)\\
&a_1\sigma^0_0 + a_2\sigma^0_1 + a_3\sigma^0_2 = S(x_1,0)\\
&\vdots\\
&\left(a_1 - a_3\tfrac{c_1}{c_3}\right)\delta^0_{N-1} + \left(a_2 - a_3\tfrac{c_2}{c_3}\right)\delta^0_N = R(x_N,0) - \tfrac{a_3}{c_3}R''(x_N,0)
\end{aligned}$$

and

$$\begin{aligned}
&\left(a_2 - a_1\tfrac{c_2}{c_1}\right)\sigma^0_0 + \left(a_3 - a_1\tfrac{c_3}{c_1}\right)\sigma^0_1 = S(x_0,0) - \tfrac{a_1}{c_1}S''(x_0,0)\\
&a_1\sigma_0 + a_2\sigma_1 + a_3\sigma_2 = S(x_1,0)\\
&\vdots\\
&\left(a_1 - a_3\tfrac{c_1}{c_3}\right)\sigma^0_{N-1} + \left(a_2 - a_3\tfrac{c_2}{c_3}\right)\sigma^0_N = S(x_N,0) - \tfrac{a_3}{c_3}S''(x_N,0).
\end{aligned}$$

Solving these systems gives the initial vector. Thus, the time-stepping scheme is ready to run, and the numerical solutions can be obtained at desired time level.

5. Consistency and truncation error analysis

In this section, the local consistency of the fully discrete scheme is examined. The following regularity is assumed; it is sufficient for the argument below, although it is not claimed to be minimal.
Assumption. The exact solution u satisfies $\partial_x^k u \in C([a,b]\times[0,T])$ for $k = 0,\dots,6$ and $u_t,\ u_{tt},\ u_{xxt} \in C([a,b]\times[0,T])$, and f_t is bounded on $[a,b]\times[0,T]$.

Let $\mathcal{T}_j^{n+1}$ denote the residual obtained when the exact solution is substituted into the discrete equations (4.14)-(4.15) before they are multiplied by $s = \Delta t^\gamma \Gamma(2-\gamma)$, with the second spatial derivative replaced by the high-order approximation $\mathcal{D}^{(4)}_{h,j}$ of Section 3.

Proposition 5.1. *Let $0 < \gamma < 1$, and assume that the exact solution of* (4.1) *satisfies the assumption above. Then, the local truncation error of the fully discrete scheme satisfies*

$$\mathcal{T}_j^{n+1} = O(\Delta t) + O(h^4). \tag{5.1}$$

Hence, the complete discretization is first-order consistent in time and fourth-order consistent in space.

Proof. For a sufficiently smooth function $v(t)$, the L1 approximation of the Caputo derivative satisfies

$${}^C D_t^\gamma v(t_{n+1}) = D^\gamma_{\Delta t} v^{n+1} + O\left(\Delta t^{\,2-\gamma}\right), \qquad 0 < \gamma < 1. \tag{5.2}$$

On the other hand, the Crank–Nicolson-type average provides a second-order approximation at the temporal midpoint. However, when expressed relative to the time level t^{n+1}, as required in the present consistency analysis, it satisfies

$$\frac{v^{n+1} + v^n}{2} = v(t_{n+1}) + O(\Delta t). \tag{5.3}$$

Although the centered average is second-order accurate at $t_{n+\frac{1}{2}}$, the L1 derivative in the present scheme is evaluated at t_{n+1}. Therefore, when the fully discrete equation is compared with the differential

equation at the same time level t_{n+1}, this difference in temporal levels introduces an $O(\Delta t)$ consistency term. Furthermore, the nonlinear coefficient is evaluated explicitly at the previous time level,

$$Z_j^n = (R_j^n)^2 + (S_j^n)^2 = Z(x_j, t_{n+1}) + O(\Delta t), \tag{5.4}$$

for a sufficiently smooth solution. Thus, the frozen treatment of the nonlinear coefficient also contributes an $O(\Delta t)$ term. Finally, the source term is evaluated at the midpoint $t_{n+\frac{1}{2}}$ in the discrete equations and at $f(x_j, t_{n+\frac{1}{2}}) = f(x_j, t_{n+1}) + O(\Delta t)$, which is again an $O(\Delta t)$ contribution. For the spatial discretization, the high-order approximation derived in Section 3 gives

$$u_{xx}(x_j, t) = \mathcal{D}_{h,j}^{(4)} u(x_j, t) + O(h^4) \tag{5.5}$$

under the stated spatial smoothness assumptions. Combining these contributions, the local residual of the complete scheme satisfies

$$\begin{aligned} \mathcal{T}_j^{n+1} &= O\left(\Delta t^{2-\gamma}\right) + O(\Delta t) + O(h^4) \\ &= O(\Delta t + h^4), \qquad 0 < \gamma < 1 \end{aligned} \tag{5.6}$$

because $2 - \gamma > 1$. This proves (5.1). □

Remark 5.2. The estimate in Proposition 5.1 is a local consistency result and should not be interpreted as a global convergence theorem. In particular, the $O(\Delta t^{2-\gamma})$ accuracy of the L1 formula alone does not determine the temporal order of the complete scheme. Owing to the temporal-level treatment of the remaining terms and the frozen nonlinear coefficient, the full discretization is first-order consistent in time. The fourth-order statement refers to the spatial discretization.

6. Fourier resolvent analysis

In this section, we investigate the Fourier resolvent associated with the linearized form of the proposed numerical scheme. Because the nonlinear coefficient depends on the numerical solution, the quantity

$$Z = R^2 + S^2$$

is frozen and regarded as a real constant during the analysis. It is important to distinguish the present analysis from the classical von Neumann amplification-factor argument. For $0 < \gamma < 1$, the L1 approximation of the Caputo derivative contains a discrete convolution involving all previous time levels. Consequently, a Fourier mode cannot in general be represented by a single time-independent amplification factor. We therefore work directly with the complete fractional convolution recurrence and its generating function.

Notation. In this section, i denotes the imaginary unit, j the spatial index, and n the time level. The numbers $b_k = (k+1)^{1-\gamma} - k^{1-\gamma}$ are the L1 weights of Section 2, and $s = \Delta t^{\gamma}\Gamma(2-\gamma)$ is the parameter introduced in Section 4. The constant Z is the frozen nonlinear coefficient. A Fourier mode of wave number θ has the amplitudes P^n and W^n for the real and imaginary parts, and $\zeta^n = P^n + \mathrm{i}W^n$ is the complex amplitude. The real symbols $A(\theta)$ and $B(\theta)$ and their ratio $\rho(\theta)$ are defined below, $\mathcal{B}_\gamma(z)$ is the generating function of the L1 weights, and $\mathcal{Z}(z)$ is the generating function of the amplitudes ζ^n.

Let

$$R_j^n = P^n e^{\mathrm{i}j\theta}, \qquad S_j^n = W^n e^{\mathrm{i}j\theta}, \tag{6.1}$$

where θ is the Fourier wave number and P^n and W^n are time-dependent Fourier amplitudes. For a symmetric B-spline basis, define

$$A(\theta) = a_2 + 2a_1 \cos\theta \tag{6.2}$$

and

$$C_4(\theta) = \frac{5 + \cos\theta}{6} \left(c_2 + 2c_1 \cos\theta\right). \tag{6.3}$$

The factor $(5 + \cos\theta)/6$ is real and positive for every θ. We further define

$$B(\theta) = \frac{s}{2} \left[C_4(\theta) + ZA(\theta)\right], \tag{6.4}$$

where s is the time-discretization parameter appearing in the fully discrete scheme. Because the spline coefficients are real and symmetric and, Z is real, both $A(\theta)$ and $B(\theta)$ are real. Substitution of (6.1) into the homogeneous linearized difference equations gives

$$A \sum_{k=0}^{n} b_k \left(W^{n-k+1} - W^{n-k}\right) = B\left(P^{n+1} + P^n\right), \tag{6.5}$$

$$A \sum_{k=0}^{n} b_k \left(P^{n-k+1} - P^{n-k}\right) = -B\left(W^{n+1} + W^n\right). \tag{6.6}$$

Introducing the complex Fourier amplitude

$$\zeta^n = P^n + \mathrm{i}W^n. \tag{6.7}$$

Equations (6.5)-(6.6) can be combined as

$$A \sum_{k=0}^{n} b_k \left(\zeta^{n-k+1} - \zeta^{n-k}\right) = \mathrm{i}B\left(\zeta^{n+1} + \zeta^n\right). \tag{6.8}$$

Equivalently,

$$(A - \mathrm{i}B)\zeta^{n+1} = (A + \mathrm{i}B)\zeta^n - A \sum_{k=1}^{n} b_k \left(\zeta^{n-k+1} - \zeta^{n-k}\right). \tag{6.9}$$

For $n = 0$, the memory sum is empty, and hence,

$$\zeta^1 = \frac{A + \mathrm{i}B}{A - \mathrm{i}B}\zeta^0. \tag{6.10}$$

Because $A, B \in \mathbb{R}$,

$$\left|\frac{A + \mathrm{i}B}{A - \mathrm{i}B}\right| = 1. \tag{6.11}$$

Equation (6.11) is only a one-step identity. In the fractional case, it must not be interpreted as a time-independent amplification factor for all subsequent time levels because the memory term in (6.9) contains the complete history of the Fourier amplitudes.

6.1. Generating function of the L1 weights

For $0 < \gamma < 1$, the L1 coefficients are

$$b_k = (k+1)^{1-\gamma} - k^{1-\gamma}, \qquad k = 0, 1, 2, \ldots. \tag{6.12}$$

Define

$$\mathcal{B}_\gamma(z) = \sum_{k=0}^{\infty} b_k z^k, \qquad |z| < 1. \tag{6.13}$$

The following positivity property will be used to locate the zeros of the Fourier resolvent denominator.

Lemma 6.1. *For* $0 < \gamma < 1$,

$$\operatorname{Re}\left[\frac{1-z}{1+z}\mathcal{B}_\gamma(z)\right] > 0, \qquad |z| < 1. \tag{6.14}$$

Proof. From (6.12),

$$b_k = (1-\gamma)\int_k^{k+1} \tau^{-\gamma}\, d\tau. \tag{6.15}$$

Using

$$\tau^{-\gamma} = \frac{1}{\Gamma(\gamma)}\int_0^\infty t^{\gamma-1} e^{-\tau t}\, dt,$$

we obtain

$$b_k = \frac{1-\gamma}{\Gamma(\gamma)}\int_0^\infty t^{\gamma-2}(1-e^{-t})e^{-kt}\, dt. \tag{6.16}$$

With $x = e^{-t}$, this can be written as

$$b_k = \int_0^1 x^k\, d\mu_\gamma(x), \tag{6.17}$$

where

$$d\mu_\gamma(x) = \frac{1-\gamma}{\Gamma(\gamma)}(1-x)(-\ln x)^{\gamma-2}\frac{dx}{x} \tag{6.18}$$

is a positive measure on $(0, 1)$. Consequently,

$$\mathcal{B}_\gamma(z) = \int_0^1 \frac{1}{1-xz}\, d\mu_\gamma(x), \qquad |z| < 1. \tag{6.19}$$

Hence,

$$\frac{1-z}{1+z}\mathcal{B}_\gamma(z) = \int_0^1 \frac{1-z}{(1+z)(1-xz)}\, d\mu_\gamma(x). \tag{6.20}$$

Let $z = a + \mathrm{i}b$. A direct calculation gives

$$\operatorname{Re}\left[\frac{1-z}{(1+z)(1-xz)}\right] = \frac{(1-|z|^2)(1-x\operatorname{Re} z) + 2x(\operatorname{Im} z)^2}{|1+z|^2|1-xz|^2}. \tag{6.21}$$

For $|z| < 1$ and $0 \le x \le 1$,

$$1 - |z|^2 > 0, \qquad \text{and} \qquad 1 - x\operatorname{Re} z \ge 1 - x|z| > 0,$$

and $2x(\operatorname{Im} z)^2 \ge 0$, and the denominator in (6.21) is strictly positive. Therefore,

$$\operatorname{Re}\left[\frac{1-z}{(1+z)(1-xz)}\right] > 0.$$

Because $d\mu_\gamma$ is a positive measure, integration in (6.20) yields (6.14). □

6.2. Fourier resolvent

Assume that $A(\theta) > 0$, as verified below for the spline bases used in this study, and define

$$\rho(\theta) = \frac{B(\theta)}{A(\theta)} \in \mathbb{R}. \tag{6.22}$$

Dividing (6.8) by A gives

$$\sum_{k=0}^{n} b_k \left(\zeta^{n-k+1} - \zeta^{n-k}\right) = \mathrm{i}\rho \left(\zeta^{n+1} + \zeta^{n}\right). \tag{6.23}$$

Introduce the generating function

$$\mathcal{Z}(z) = \sum_{n=0}^{\infty} \zeta^n z^n. \tag{6.24}$$

Using

$$\sum_{n=0}^{\infty} (\zeta^{n+1} - \zeta^n) z^n = \frac{(1-z)\mathcal{Z}(z) - \zeta^0}{z} \tag{6.25}$$

and

$$\sum_{n=0}^{\infty} (\zeta^{n+1} + \zeta^n) z^n = \frac{(1+z)\mathcal{Z}(z) - \zeta^0}{z}, \tag{6.26}$$

the generating-function form of (6.23) becomes

$$\mathcal{B}_\gamma(z) \left[(1-z)\mathcal{Z}(z) - \zeta^0\right] = \mathrm{i}\rho \left[(1+z)\mathcal{Z}(z) - \zeta^0\right]. \tag{6.27}$$

Therefore,

$$\mathcal{Z}(z) = \zeta^0 \frac{\mathcal{B}_\gamma(z) - \mathrm{i}\rho}{(1-z)\mathcal{B}_\gamma(z) - \mathrm{i}\rho(1+z)}. \tag{6.28}$$

Define

$$\Delta_\rho(z) = (1-z)\mathcal{B}_\gamma(z) - \mathrm{i}\rho(1+z). \tag{6.29}$$

Theorem 6.2. *Let $0 < \gamma < 1$, let $\rho \in \mathbb{R}$, and assume $A(\theta) > 0$. Then,*

$$\Delta_\rho(z) \neq 0, \qquad |z| < 1. \tag{6.30}$$

Thus, the Fourier resolvent has no pole in the open unit disk for any real value of the Fourier parameter ρ.

Proof. Suppose that

$$\Delta_\rho(z) = 0$$

for some $|z| < 1$. Then,

$$(1-z)\mathcal{B}_\gamma(z) = \mathrm{i}\rho(1+z).$$

Because $1 + z \neq 0$ in the open unit disk,

$$\frac{1-z}{1+z}\mathcal{B}_\gamma(z) = \mathrm{i}\rho. \tag{6.31}$$

The right-hand side has zero real part because $\rho \in \mathbb{R}$, whereas Lemma 6.1 gives

$$\operatorname{Re}\left[\frac{1-z}{1+z}\mathcal{B}_\gamma(z)\right] > 0.$$

This is a contradiction. Hence

$$\Delta_\rho(z) \neq 0, \qquad |z| < 1.$$

□

Remark 6.3. Theorem 6.2 concerns the location of the poles of the discrete Fourier resolvent. No condition coupling the temporal step size with the spatial mesh size is required to establish (6.30). However, pole-freeness of the generating function in the open unit disk does not by itself provide a uniform bound on its Taylor coefficients. Therefore, Theorem 6.2 is not interpreted as a proof of unconditional stability in the stronger sense

$$\sup_{n\geq 0} |\zeta^n| \leq C|\zeta^0|.$$

Accordingly, no unconditional stability claim is made for the fractional scheme on the basis of the present resolvent analysis.

6.3. Behavior on the boundary and at $\rho = 0$

The zeros of Δ_ρ are also excluded on the unit circle itself. For $z = e^{\mathrm{i}\varphi}$ with $0 < |\varphi| < \pi$, the same moment representation (6.19) gives

$$\operatorname{Im}\mathcal{B}_\gamma(e^{\mathrm{i}\varphi}) = \sin\varphi \int_0^1 \frac{x}{|1-xe^{\mathrm{i}\varphi}|^2}\, d\mu_\gamma(x),$$

and, because

$$\frac{1-e^{\mathrm{i}\varphi}}{1+e^{\mathrm{i}\varphi}} = -\mathrm{i}\tan\frac{\varphi}{2},$$

we obtain

$$\operatorname{Re}\left[\frac{1-e^{\mathrm{i}\varphi}}{1+e^{\mathrm{i}\varphi}}\mathcal{B}_\gamma(e^{\mathrm{i}\varphi})\right] = (1-\cos\varphi)\int_0^1 \frac{x}{|1-xe^{\mathrm{i}\varphi}|^2}\, d\mu_\gamma(x) > 0.$$

Therefore,

$$\Delta_\rho(e^{\mathrm{i}\varphi}) \neq 0, \qquad 0 < |\varphi| < \pi.$$

At $z = -1$,

$$\Delta_\rho(-1) = 2\mathcal{B}_\gamma(-1) = 2\int_0^1 \frac{1}{1+x}\, d\mu_\gamma(x) > 0.$$

For $\rho \neq 0$, as $z \to 1$ from within the unit disk,

$$(1-z)\mathcal{B}_\gamma(z) \to 0, \qquad -\mathrm{i}\rho(1+z) \to -2\mathrm{i}\rho,$$

so the limiting denominator remains nonzero. When $\rho = 0$, (6.23) reduces to

$$\sum_{k=0}^{n} b_k\left(\zeta^{n-k+1} - \zeta^{n-k}\right) = 0.$$

Starting from $n = 0$ and proceeding recursively gives

$$\zeta^n = \zeta^0, \qquad n \geq 0.$$

Thus, the zero-symbol mode is represented by the constant Fourier sequence.

6.4. Positivity of the spatial symbol

It remains to confirm $A(\theta) > 0$ for the spline families of Section 2. For the cubic B-spline,

$$A(\theta) = 4 + 2\cos\theta \geq 2 > 0$$

for every θ. For the trigonometric cubic B-spline, using $a_2 = 4a_1\cos(h/2)$ from Section 2, we obtain

$$A(\theta) = 2a_1\left[\cos\theta + 2\cos\left(\frac{h}{2}\right)\right].$$

Under the admissible mesh condition

$$0 < h < \frac{2\pi}{3},$$

we have $a_1 > 0$ and $2\cos(h/2) - 1 > 0$, and hence, $A(\theta) > 0$. For the uniform hyperbolic polynomial B-spline, $a_1, a_2 > 0$ for $h > 0$. Moreover,

$$A(\theta) \geq a_2 - 2a_1 = \frac{h(\cosh h + 1) - 2\sinh h}{h(\cosh h - 1)} > 0,$$

where the last inequality follows by writing $h = 2y$ and using the monotonicity of $y\cosh y - \sinh y$ for $y > 0$. Thus, $A(\theta) > 0$ holds for all three spline families under their respective admissible mesh conditions, and consequently,

$$\rho(\theta) = \frac{B(\theta)}{A(\theta)}$$

is real and finite for every Fourier mode. The restriction $0 < h < 2\pi/3$ for the trigonometric cubic B-spline is a spatial admissibility condition on the spline coefficients, not a Courant–Friedrichs–Lewy (CFL) type condition coupling Δt and h.

6.5. Classical limit $\gamma = 1$

For $\gamma = 1$, the memory term disappears, and (6.23) reduces to

$$\zeta^{n+1} - \zeta^n = \mathrm{i}\rho(\zeta^{n+1} + \zeta^n).$$

Hence,

$$\zeta^{n+1} = \frac{1 + \mathrm{i}\rho}{1 - \mathrm{i}\rho}\zeta^n,$$

with

$$\left|\frac{1 + \mathrm{i}\rho}{1 - \mathrm{i}\rho}\right| = 1.$$

Thus, the usual neutral Fourier stability property of the classical Crank–Nicolson limit is recovered for $\gamma = 1$.

7. Numerical results

In this section, the performance of the proposed numerical method is investigated through three test problems. The accuracy and reliability of the method are evaluated by considering the L_2 and L_∞ error norms, convergence rates, and comparisons with existing numerical results reported in the literature. In addition, temporal and spatial refinement studies are considered separately in order to examine the consistency behavior discussed in Section 5. The first two test problems involve sufficiently smooth solutions, whereas the third problem involves a solution with limited temporal regularity and is used to investigate the numerical behavior of the method in the presence of a weak initial singularity.

For the numerical experiments, the computational domain is divided into a uniform mesh with spatial step size h and time step size Δt. The accuracy of the proposed scheme is measured using the following error norms:

$$L_2 = \left(h \sum_{j=0}^{N} |u_j - U_j|^2 \right)^{1/2},$$

and

$$L_\infty = \max_{0 \le j \le N} |u_j - U_j|,$$

where u_j and U_j represent the exact and numerical solutions, respectively, at the nodal points (x_j, t_n).

The rate of convergence (RoC) is calculated by

$$\text{RoC} = \frac{\log(E_{q_1}/E_{q_2})}{\log(q_1/q_2)},$$

where E_q denotes the corresponding error norm, and q represents the refinement parameter. Thus, $q = h$ is used for the spatial convergence tests, whereas $q = \Delta t$ is used for the temporal convergence tests.

7.1. Problem 1

As a first test problem, the time-fractional nonlinear Schrödinger equation

$$i\frac{\partial^\gamma u}{\partial t^\gamma} + \frac{\partial^2 u}{\partial x^2} + |u|^2 u = f(x,t), \quad 0 < \gamma \le 1, \text{ and } t \ge 0 \tag{7.1}$$

is considered on the interval $[0, 1]$ with the boundary conditions

$$u(0,t) = it^2, \quad u(1,t) = it^2, \quad t \ge 0 \tag{7.2}$$

and the initial condition

$$u(x,0) = 0. \tag{7.3}$$

The exact solution of this problem is

$$u(x,t) = t^2 \left(\sin(2\pi x) + i\cos(2\pi x)\right), \tag{7.4}$$

and the corresponding source term is

$$f(x,t) = -2\frac{t^{2-\gamma}}{\Gamma(3-\gamma)}\cos(2\pi x) + (t^6 - 4\pi^2 t^2)\sin(2\pi x) + i\left(2\frac{t^{2-\gamma}}{\Gamma(3-\gamma)}\sin(2\pi x) + (t^6 - 4\pi^2 t^2)\cos(2\pi x)\right). \tag{7.5}$$

Tables 1 and 2 present the numerical and exact solutions of the real and imaginary parts, respectively, obtained with $N = 50$, $\Delta t = 0.001$, and $t_f = 1$ for $\gamma = 0.1, 0.3, 0.7, 0.9$. The numerical solutions are in close agreement with the exact solution for all considered values of the fractional order. For the real part, the L_2 and L_∞ errors remain small for all tested values of γ. The pointwise errors vary slightly with the fractional order and spatial position, without showing a uniform monotonic dependence on γ.

For the imaginary part, the errors remain small over the considered values of γ. Both error norms decrease as γ increases, with L_∞ decreasing from approximately 1.39×10^{-4} at $\gamma = 0.1$ to approximately 1.00×10^{-4} at $\gamma = 0.9$. Overall, Tables 1 and 2 show that the numerical solution remains close to the exact solution for all tested values of the fractional order.

Table 1. Comparison of numerical and exact solutions for the real part of Problem 1 for $N = 50$, $\Delta t = 0.001$, $t_f = 1$, and different values of γ.

x	$\gamma = 0.1$	$\gamma = 0.3$	$\gamma = 0.7$	$\gamma = 0.9$	Exact solution
0.0	0.000000	0.000000	0.000000	0.000000	0.000000
0.1	0.587755	0.587754	0.587748	0.587743	0.587785
0.2	0.951017	0.951015	0.951003	0.950989	0.951057
0.3	0.951031	0.951028	0.951011	0.950988	0.951057
0.4	0.587792	0.587788	0.587768	0.587737	0.587785
0.5	0.000045	0.000041	0.000019	−0.000015	0.000000
0.6	−0.587711	−0.587715	−0.587736	−0.587768	−0.587785
0.7	−0.950974	−0.950977	−0.950995	−0.951020	−0.951057
0.8	−0.950989	−0.950991	−0.951004	−0.951019	−0.951057
0.9	−0.587749	−0.587751	−0.587757	−0.587763	−0.587785
1.0	0.000000	0.000000	0.000000	0.000000	0.000000
L_2	4.82899135$e-05$	4.68923843$e-05$	4.09051615$e-05$	4.14293819$e-05$	
L_∞	8.28566013$e-05$	7.95722606$e-05$	6.18037040$e-05$	7.13536981$e-05$	

Table 2. Comparison of numerical and exact solutions for the imaginary part of Problem 1 for $N = 50$, $\Delta t = 0.001$, $t_f = 1$, and different values of γ.

x	$\gamma = 0.1$	$\gamma = 0.3$	$\gamma = 0.7$	$\gamma = 0.9$	Exact solution
0.0	1.000000	1.000000	1.000000	1.000000	1.000000
0.1	0.809050	0.809050	0.809043	0.809030	0.809017
0.2	0.309093	0.309092	0.309080	0.309058	0.309017
0.3	−0.308902	−0.308903	−0.308919	−0.308945	−0.309017
0.4	−0.808880	−0.808881	−0.808898	−0.808922	−0.809017
0.5	−0.999866	−0.999868	−0.999883	−0.999901	−1.000000
0.6	−0.808910	−0.808912	−0.808924	−0.808933	−0.809017
0.7	−0.308950	−0.308953	−0.308961	−0.308963	−0.309017
0.8	0.309044	0.309043	0.309038	0.309040	0.309017
0.9	0.809020	0.809019	0.809017	0.809019	0.809017
1.0	1.000000	1.000000	1.000000	1.000000	1.000000
L_2	$8.56477485e-05$	$8.45880849e-05$	$7.38200661e-05$	$6.03052743e-05$	
L_∞	$1.38863425e-04$	$1.37467045e-04$	$1.21277943e-04$	$1.00218596e-04$	

Tables 3 and 4 report the numerical and exact solutions of the real and imaginary parts for $\Delta t = 0.002$, $t_f = 1$, and $\gamma = 0.5$ to examine the behavior of the spatial discretization. The time step is kept fixed, and only the spatial mesh is refined, with the number of subintervals increased through $N = 10, 20, 40, 80$. For the real part, the L_2 error drops from nearly 3.52×10^{-4} at $N = 10$ to nearly 1.03×10^{-4} at $N = 20$, and the imaginary part improves more sharply, from nearly 1.07×10^{-3} to nearly 2.04×10^{-4} over the same refinement. However, for $N = 40$ and $N = 80$, the errors show only minor variations; for example, the real part L_2 norm changes only from 8.88×10^{-5} to 8.79×10^{-5} between $N = 40$ and $N = 80$. Because Δt is kept constant, the temporal error remains fixed while the spatial error decreases with increasing N. Therefore, further spatial refinement produces no significant reduction in the total error, indicating that the remaining error is increasingly dominated by the temporal discretization error associated with the fixed value of Δt.

Tables 5 and 6 show the error norms and temporal convergence rates of the real and imaginary parts for a fixed spatial mesh $N = 40$ at $t = 0.25$ with $\gamma = 0.5$, whereas the time step is reduced from $\Delta t = 0.01$ to $\Delta t = 0.001$. The spatial mesh is kept fixed so that the effect of temporal refinement on the accuracy of the scheme can be observed. It can be seen from the tables that both error norms decrease steadily as Δt is refined. For the real part, the L_2 error decreases from approximately 1.56×10^{-4} at $\Delta t = 0.01$ to approximately 1.66×10^{-5} at $\Delta t = 0.001$, and for the imaginary part, it decreases from approximately 1.10×10^{-4} to approximately 1.04×10^{-5}. The computed convergence rates remain close to one for both components. This numerical behavior is consistent with the first-order temporal consistency of the complete discretization discussed in Section 5. For $\gamma = 0.5$, the L1 formula alone would give the rate $2-\gamma = 1.5$; the observed rates close to one show that the temporal order of the complete scheme is determined by the time-level treatment of the remaining terms and not by the L1 formula.

Table 3. Comparison of numerical and exact solutions for the real part of Problem 1 for $\Delta t = 0.002$, $t_f = 1$, $\gamma = 0.5$, and different values of N.

x	$N = 10$	$N = 20$	$N = 40$	$N = 80$	Exact solution
0.0	0.000000	0.000000	0.000000	0.000000	0.000000
0.1	0.587553	0.587699	0.587717	0.587718	0.587785
0.2	0.950494	0.950930	0.950963	0.950965	0.951057
0.3	0.950410	0.950950	0.950986	0.950988	0.951057
0.4	0.587281	0.587748	0.587776	0.587778	0.587785
0.5	−0.000214	0.000053	0.000066	0.000067	0.000000
0.6	−0.587698	−0.587656	−0.587659	−0.587660	−0.587785
0.7	−0.950791	−0.950896	−0.950910	−0.950912	−0.951057
0.8	−0.950799	−0.950918	−0.950936	−0.950937	−0.951057
0.9	−0.587733	−0.587711	−0.587722	−0.587722	−0.587785
1.0	0.000000	0.000000	0.000000	0.000000	0.000000
L_2	$3.51638218e-04$	$1.03011279e-04$	$8.87767261e-05$	$8.79066063e-05$	
L_∞	$6.46794844e-04$	$1.60739592e-04$	$1.46025816e-04$	$1.45080618e-04$	

Table 4. Comparison of numerical and exact solutions for the imaginary part of Problem 1 for $\Delta t = 0.002$, $t_f = 1$, $\gamma = 0.5$, and different values of N.

x	$N = 10$	$N = 20$	$N = 40$	$N = 80$	Exact solution
0.0	1.000000	1.000000	1.000000	1.000000	1.000000
0.1	0.809518	0.809091	0.809079	0.809078	0.809017
0.2	0.309831	0.309188	0.309080	0.309160	0.309017
0.3	−0.307812	−0.308752	−0.308797	−0.308800	−0.309017
0.4	−0.807513	−0.808694	−0.808755	−0.808758	−0.809017
0.5	−0.998399	−0.999678	−0.999744	−0.999748	−1.000000
0.6	−0.807560	−0.808753	−0.808814	−0.808818	−0.809017
0.7	−0.307886	−0.308847	−0.308894	−0.308897	−0.309017
0.8	0.309758	0.309093	0.309064	0.309063	0.309017
0.9	0.809472	0.809032	0.809019	0.809018	0.809017
1.0	1.000000	1.000000	1.000000	1.000000	1.000000
L_2	$1.06542121e-03$	$2.04451254e-04$	$1.62991288e-04$	$1.60635816e-04$	
L_∞	$1.60074768e-03$	$3.30377110e-04$	$2.65532336e-04$	$2.62210047e-04$	

Table 5. Error norms and temporal convergence rates for the real part of Problem 1 for $N = 40$, $t = 0.25$, $\gamma = 0.5$, and different values of Δt.

Δt	L_2	RoC	L_∞	RoC
0.0100	$1.56445811e-04$	–	$2.56989099e-04$	–
0.0050	$8.03399890e-05$	0.962	$1.31936913e-04$	0.962
0.0025	$4.09332489e-05$	0.973	$6.70326467e-05$	0.977
0.0020	$3.29022105e-05$	0.979	$5.38565582e-05$	0.981
0.0010	$1.66354421e-05$	0.984	$2.72162141e-05$	0.985

Table 6. Error norms and temporal convergence rates for the imaginary part of Problem 1 for $N = 40$, $t = 0.25$, $\gamma = 0.5$, and different values of Δt.

Δt	L_2	RoC	L_∞	RoC
0.0100	$1.09615721e-04$	–	$1.90264776e-04$	–
0.0050	$5.27381458e-05$	1.056	$8.99652352e-05$	1.080
0.0025	$2.60415843e-05$	1.018	$4.37954386e-05$	1.039
0.0020	$2.08164620e-05$	1.003	$3.49094790e-05$	1.018
0.0010	$1.04292037e-05$	0.997	$1.73879718e-05$	1.006

Table 7 compares the error norms obtained by the present method with previously reported numerical results for the same test problem.

Table 7. Comparison of the L_∞ error norms of the present method with those reported in the literature for Problem 1 for $N = 40$, $t = 1$, $\Delta t = 0.002$.

	$\gamma = 0.1$		$\gamma = 0.3$	
L_∞	Real part	Imaginary part	Real part	Imaginary part
Present method	$1.6594e-04$	$2.7894e-04$	$1.5922e-04$	$2.7599e-04$
[29](Collocation)	$4.2147e-04$	$4.8592e-04$	$4.7631e-04$	$4.5151e-04$
[29] (Galerkin)	$2.8117e-03$	$5.4323e-03$	$2.9432e-03$	$5.3688e-03$
[10]	$2.8536e-03$	$2.1753e-03$	$2.8610e-03$	$2.1771e-03$

Under the parameter settings listed in Table 7, the present computations produce errors that are comparable to, and in several cases smaller than, the reported values. These comparisons provide a numerical reference for the performance of the proposed method. However, because the compared approaches may differ in their spatial and temporal discretizations, parameter choices, and implementations, the results should not be interpreted as a general ranking of the numerical methods. Table 8 presents the spatial convergence behavior of the method for $\gamma = 0.5$ at $t_f = 1$. In this experiment, a sufficiently small time step, $\Delta t = 0.00005$, is kept fixed as the spatial mesh is refined from $N = 5$ to $N = 20$. The errors decrease rapidly with spatial refinement. For the real part, the observed L_∞ convergence rates are approximately 4.18 and 3.86, whereas for the imaginary part, they are approximately 3.92 and 4.14. Thus, the observed spatial rates are close to four and are consistent with the fourth-order spatial consistency of the high-order approximation discussed in Section 5.

Table 8. Maximum error norms and convergence rates for the real and imaginary parts of Problem 1 for $t = 1$, $\Delta t = 0.00005$, $\gamma = 0.5$, and different values of N.

N	$L_\infty(R)$	RoC	$L_\infty(S)$	RoC
5	$1.05290500e-02$	–	$2.05251653e-02$	–
10	$5.80349703e-04$	4.18	$1.35728154e-03$	3.92
20	$4.00974039e-05$	3.86	$7.70858771e-05$	4.14

Table 9 extends the spatial convergence check of Table 8 to $N = 40$ and to a smaller time step for the real part. The observed rates (3.89 and 3.52 for $\Delta t = 2.5\times10^{-5}$; 3.90 and 3.74 for $\Delta t = 1.25\times10^{-5}$) remain close to four but decrease slightly between $N = 20$ and $N = 40$; this is consistent with the fixed

time step contributing a temporal error of $O(\Delta t)$, whose relative weight grows as the $O(h^4)$ spatial error shrinks. Halving Δt reduces this contamination and brings the observed rate closer to four, as seen in the table.

Table 9. Maximum absolute errors and spatial convergence rates for the real part of Problem 1 with $\gamma = 0.5$ and $t_f = 1$, using two sufficiently small fixed time steps.

Δt	$N = 10$	$N = 20$	RoC	$N = 40$	RoC
0.000025	$5.7953e-04$	$3.9178e-05$	3.89	$3.4240e-06$	3.52
0.0000125	$5.7912e-04$	$3.8766e-05$	3.90	$2.9008e-06$	3.74

Tables 10 and 11 present additional refinement experiments in which the time step is selected according to the balanced refinement relation $\Delta t = Ch^4$ so that the first-order temporal consistency error $O(\Delta t)$ and the fourth-order spatial consistency error $O(h^4)$ are of the same order. Under this joint-refinement strategy, both contributions to the local consistency error discussed in Section 5 scale as $O(h^4)$, and the observed convergence rates are therefore expected to approach four as the mesh is refined.

Table 10. Maximum absolute errors and convergence rates for the real part of Problem 1 under the joint-refinement strategy $\Delta t = Ch^4$, with $\gamma = 0.8$ and $t_f = 1$.

N	Δt	L_∞	RoC
10	1/5	1.9210290694e-02	–
20	1/80	8.4453392092e-04	4.51
40	1/1280	4.7941553789e-05	4.13
80	1/20480	2.8869101609e-06	4.05

Table 11. Maximum absolute errors and convergence rates for the imaginary part of Problem 1 under the joint-refinement strategy $\Delta t = Ch^4$, with $\gamma = 0.5$ and $t_f = 1$.

N	Δt	L_∞	RoC
10	1/5	3.5386701584e-02	–
20	1/80	1.7456730670e-03	4.34
40	1/1280	1.0591314509e-04	4.04
80	1/20480	6.6181057330e-06	4.00

As shown in Tables 10 and 11, the observed rates approach four as N increases for both the real and the imaginary parts ($4.51 \to 4.13 \to 4.05$ and $4.34 \to 4.04 \to 4.00$, respectively). These results are consistent with the combined error behavior predicted by the local consistency analysis of Section 5 under the relation $\Delta t = Ch^4$. Tables 12 and 13 present numerical results obtained using cubic, trigonometric cubic, and uniform hyperbolic polynomial B-spline bases. In both tables, the time step is small enough, $\Delta t = 0.000025$, for the spatial error to be visible, and the two tables use identical parameters ($\gamma = 0.8$; $t_f = 0.5$; $N = 4, 8, 16$), differing only in the solution component considered.

Table 12. Comparison of the L_2 and L_∞ error norms for the real part of Problem 1 using different B-spline bases at $t_f = 0.5$, $\gamma = 0.8$, and $\Delta t = 0.000025$ for various values of N.

	Trigonometric	Cubic	Hyperbolic
$N = 4$			
L_2	$6.9770270065e-03$	$5.1211056908e-03$	$4.4846383633e-03$
L_∞	$1.0113925127e-02$	$8.2497282110e-03$	$7.5086940099e-03$
$N = 8$			
L_2	$4.9398668344e-04$	$1.8774987329e-04$	$4.1336658991e-04$
L_∞	$7.6494319840e-04$	$3.3450056310e-04$	$7.3300402285e-04$
$N = 16$			
L_2	$1.4866601699e-04$	$1.2843672021e-05$	$7.7637089231e-05$
L_∞	$2.5364903384e-04$	$2.2715519706e-05$	$1.3347330006e-04$

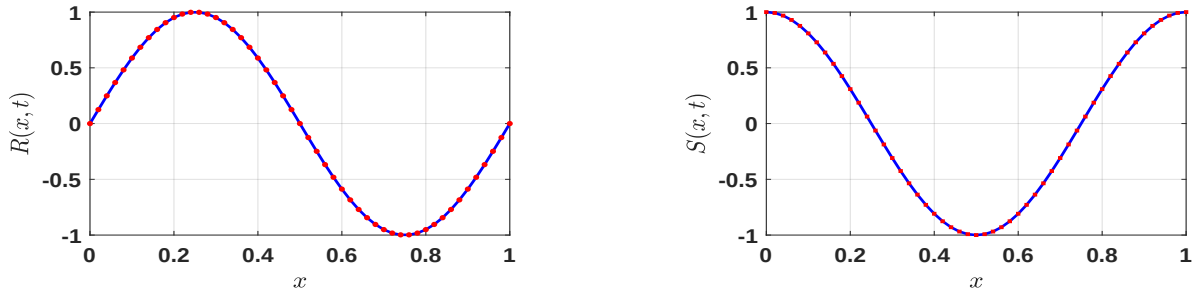
From $N = 4$ to $N = 8$ and from $N = 8$ to $N = 16$, the observed L_2 rates are 4.77 and 3.87 for the cubic B-spline, 3.82 and 1.73 for the trigonometric cubic B-spline, and 3.44 and 2.41 for the uniform hyperbolic polynomial B-spline; only the cubic B-spline remains close to the fourth order at the finer mesh. Table 13 reports the corresponding errors for the imaginary part. The relative errors of the three spline bases again depend on the spatial discretization.

Table 13. Comparison of the error norms for the imaginary part of Problem 1 using cubic, trigonometric cubic, and uniform hyperbolic polynomial B-spline bases for $\gamma = 0.8$, $\Delta t = 0.000025$, $t_f = 0.5$, and different values of N.

	Trigonometric	Cubic	Hyperbolic
$N = 4$			
L_2	$9.6451326787e-04$	$3.7694810857e-03$	$4.9365467020e-03$
L_∞	$1.4442817515e-03$	$6.1702942393e-03$	$8.1090626111e-03$
$N = 8$			
L_2	$4.4598858053e-04$	$4.7542709947e-04$	$8.2685263799e-04$
L_∞	$7.8176697428e-04$	$6.8625353072e-04$	$1.2739755871e-03$
$N = 16$			
L_2	$2.0817059452e-04$	$2.2675962059e-05$	$1.1523404335e-04$
L_∞	$3.4370847415e-04$	$3.5518774642e-05$	$1.8789394904e-04$

For $N = 4$, the trigonometric cubic B-spline produces the smallest reported errors, whereas at $N = 16$, the smallest reported errors are obtained with the cubic B-spline. Thus, the relative error levels of the three bases vary with the discretization parameters considered. Between $N = 4$ and $N = 16$, the observed L_2 rates are 2.99 and 4.39 for the cubic B-spline, 1.11 and 1.10 for the trigonometric cubic B-spline, and 2.58 and 2.84 for the uniform hyperbolic polynomial B-spline. Thus, only the cubic B-spline approaches the fourth order in this experiment, in agreement with the fact that the analysis of Section 5 concerns the corrected cubic B-spline approximation. It should be emphasized that the fourth-order spatial consistency analysis presented in Section 5 is associated with the corrected cubic B-spline spatial approximation. The trigonometric cubic and uniform hyperbolic polynomial B-spline results in Tables 12 and 13 are included only as numerical comparisons; no identical fourth-

order consistency property is inferred for these alternative bases from the cubic B-spline analysis. The graphical results for Problem 1 are provided to visualize the behavior of the numerical solution and the numerical error. Figure 1 compares the numerical and exact solutions of the real and imaginary parts of Problem 1, obtained with $N = 50$, $\Delta t = 0.001$, and $\gamma = 0.5$ at $t_f = 1$. Consistent with the small error norms reported in the tables, the differences between the numerical and exact solutions are not visually distinguishable, and the corresponding curves nearly overlap for both the real and imaginary parts.



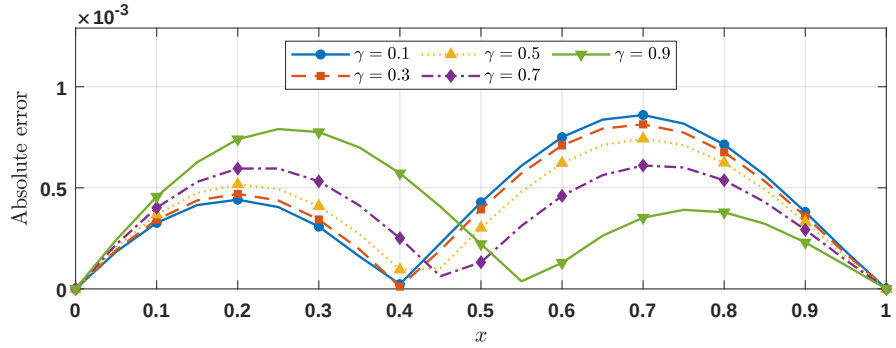
(a) Real part **(b)** Imaginary part

Figure 1. Comparison of the numerical solution (circles) and the exact solution (solid line) for the real and imaginary parts of Problem 1 for $N = 50$, $\Delta t = 0.001$, and $\gamma = 0.5$ at $t_f = 1$.

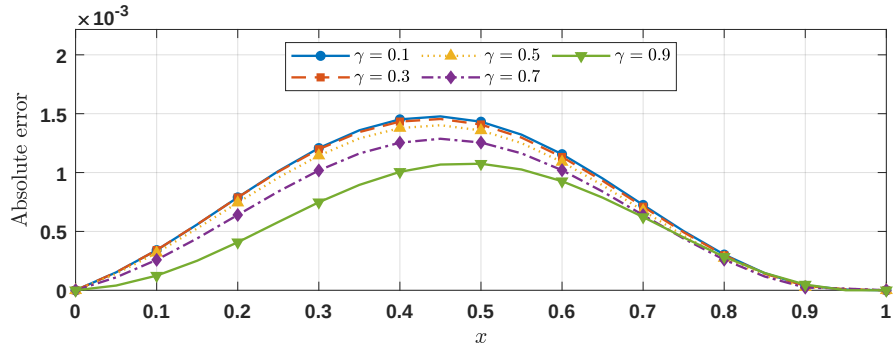
Figure 2a,2b depicts the distribution of the absolute errors along the domain at $t = 1$ for the real and imaginary parts of Problem 1, respectively, for $N = 20$; $\Delta t = 0.01$; and $\gamma = 0.1, 0.3, 0.5, 0.7, 0.9$. In these figures, the error is zero at the two endpoints of the domain in accordance with the prescribed boundary conditions and increases in the interior. The error of the real part exhibits two dominant peaks located in the first and second halves of the interval. The ordering of the curves with respect to γ changes across the domain. Near the first peak, the error is largest for $\gamma = 0.9$ and smallest for $\gamma = 0.1$, whereas near the second peak, this ordering is reversed. For the imaginary part, a single dominant peak appears in the interior of the interval. The maximum error is obtained for $\gamma = 0.1$, and the error generally decreases as γ increases, with $\gamma = 0.9$ producing the smallest error over most of the interval. These plots indicate that for this test problem, the fractional order affects not only the magnitude but also the spatial distribution of the numerical error.

Figure 3a,3b presents the numerical solution of Problem 1 as surfaces over the space–time plane for the real and imaginary parts, respectively, obtained with $N = 20$, $\Delta t = 0.01$, and $\gamma = 0.5$. Both surfaces start from the zero initial condition at $t = 0$ and gradually develop the spatial profile of the solution as time increases. For the real part, the solution develops a positive peak in the first half of the interval and a negative peak in the second half. The imaginary part develops the corresponding spatial profile with increasing amplitude as time increases, in accordance with the t^2 dependence of the exact solution.

Figure 4 shows the L_∞ error against the mesh size h on a logarithmic scale for the real and imaginary parts of Problem 1, with $\gamma = 0.5$ and $\Delta t = 0.00005$. The error curves are approximately parallel to the reference line of slope four. This behavior is consistent with the approximately fourth-order spatial rates reported in Table 8 and with the fourth-order spatial consistency of the high-order approximation discussed in Section 5.

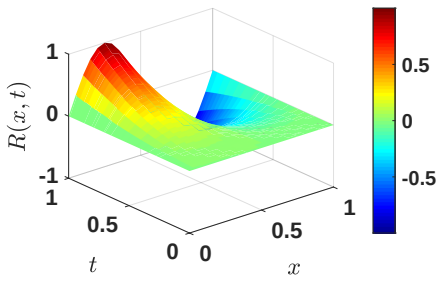


(a) Real part

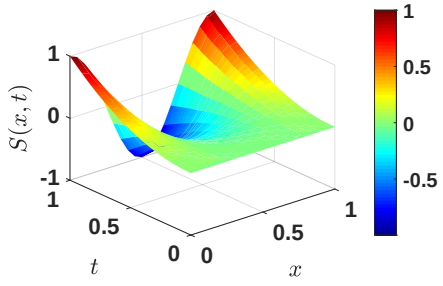


(b) Imaginary part

Figure 2. Distribution of the absolute error at $t = 1$ for the real part (top) and the imaginary part (bottom) of Problem 1 for $N = 20$; $\Delta t = 0.01$; and $\gamma = 0.1, 0.3, 0.5, 0.7, 0.9$.



(a) Real part



(b) Imaginary part

Figure 3. Space–time surfaces of the numerical solution for the real part (left) and the imaginary part (right) of Problem 1 for $N = 20$, $\Delta t = 0.01$, and $\gamma = 0.5$.

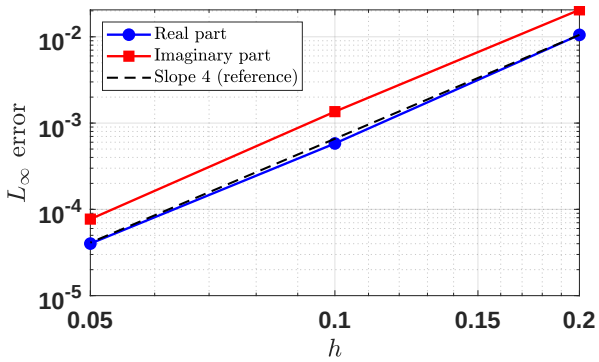


Figure 4. L_∞ error versus mesh size h for the real and imaginary parts of Problem 1 for $\gamma = 0.5$ and $\Delta t = 0.00005$. The dashed reference line has slope four.

In none of the computations reported in this section was a spurious oscillation observed, and for Problem 1, the error is largest at the final time decreases with the time step, and the error distributions in Figure 2a,2b show no oscillations. Additional computations for Problem 1 with $\gamma = 0.5$ and $N = 100$ show, however, that for a longer final time, the time step must be sufficiently small. At $t_f = 1.5$, the error decreases, with the time step with rates approaching one. At $t_f = 2$, where the exact solution has modulus $|u| = 4$, the errors at $\Delta t = 0.05$ and $\Delta t = 0.00625$ are 25 and 0.16, respectively, that is, larger than the solution itself in the first case. This is consistent with the explicit treatment of the nonlinear coefficient and with the fact that no unconditional stability is claimed. These are numerical observations and do not constitute a stability analysis of the nonlinear scheme.

7.2. Problem 2

As a second test problem, the time-fractional nonlinear Schrödinger equation (1.1) is considered on $[0, 1] \times [0, 1]$ with the initial condition

$$u(x, 0) = 0 \tag{7.6}$$

and the boundary conditions

$$u(0, t) = 0, \quad u(1, t) = it^2, \quad t \geq 0. \tag{7.7}$$

For this problem, the exact solution is taken as

$$u(x, t) = t^2 \left((1 - x)x + ix^2\right), \tag{7.8}$$

and the corresponding source term is

$$\begin{aligned} f(x, t) = &-2\frac{t^{2-\gamma}}{\Gamma(3-\gamma)}x^2 - 2t^2 + t^6x^3(1 - x)\left((1 - x)^2 + x^2\right) \\ &+i\left(2\frac{t^{2-\gamma}}{\Gamma(3-\gamma)}(1 - x)x + t^6x^4\left(x^2 + (1 - x)^2\right) + 2t^2\right). \end{aligned} \tag{7.9}$$

Tables 14 and 15 present the numerical and exact solutions of the real and imaginary parts of Problem 2 for $N = 50$, $\Delta t = 0.001$, and $t_f = 1$ at $\gamma = 0.1, 0.3, 0.7, 0.9$. At every node, the numerical values are in close agreement with the exact solution. For the real part, the error norms remain of order 10^{-5} for all the fractional orders considered. Although the errors do not vary monotonically with γ, the

smallest errors among the reported values are obtained at $\gamma = 0.9$, where the L_∞ error is approximately 2.17×10^{-5}. For the imaginary part, the L_2 errors are of order 10^{-6}, and the smallest reported L_2 and L_∞ errors occur at $\gamma = 0.7$. Overall, the errors in the imaginary part are smaller than those in the real part for the parameter values considered in these tables.

Table 14. Comparison of numerical and exact solutions for the real part of Problem 2 for $N = 50$, $\Delta t = 0.001$, $t_f = 1$, and different values of γ.

x	$\gamma = 0.1$	$\gamma = 0.3$	$\gamma = 0.7$	$\gamma = 0.9$	Exact solution
0.0	0.000000	0.000000	0.000000	0.000000	0.000000
0.1	0.089989	0.089989	0.089991	0.089996	0.090000
0.2	0.159979	0.159978	0.159982	0.159992	0.160000
0.3	0.209968	0.209968	0.209973	0.209988	0.210000
0.4	0.239960	0.239959	0.239965	0.239985	0.240000
0.5	0.249953	0.249952	0.249959	0.249981	0.250000
0.6	0.239950	0.239948	0.239956	0.239979	0.240000
0.7	0.209951	0.209950	0.209957	0.209978	0.210000
0.8	0.159959	0.159958	0.159963	0.159981	0.160000
0.9	0.089975	0.089974	0.089977	0.089988	0.090000
1.0	0.000000	0.000000	0.000000	0.000000	0.000000
L_2	$3.56792198e-05$	$3.65377059e-05$	$3.11821228e-05$	$1.48657113e-05$	
L_∞	$5.05826846e-05$	$5.18186398e-05$	$4.43990342e-05$	$2.16502256e-05$	

Table 15. Comparison of numerical and exact solutions for the imaginary part of Problem 2 for $N = 50$, $\Delta t = 0.001$, $t_f = 1$, and different values of γ.

x	$\gamma = 0.1$	$\gamma = 0.3$	$\gamma = 0.7$	$\gamma = 0.9$	Exact solution
0.0	0.000000	0.000000	0.000000	0.000000	0.000000
0.1	0.010003	0.010003	0.010003	0.010000	0.010000
0.2	0.040004	0.040005	0.040005	0.040000	0.040000
0.3	0.090005	0.090006	0.090006	0.089999	0.090000
0.4	0.160003	0.160004	0.160005	0.159997	0.160000
0.5	0.250000	0.250001	0.250002	0.249994	0.250000
0.6	0.359995	0.359997	0.359997	0.359990	0.360000
0.7	0.489990	0.489991	0.489992	0.489985	0.490000
0.8	0.639987	0.639988	0.639988	0.639983	0.640000
0.9	0.809988	0.809988	0.809989	0.809986	0.810000
1.0	1.000000	1.000000	1.000000	1.000000	1.000000
L_2	$6.94585694e-06$	$6.76920894e-06$	$6.64516796e-06$	$9.17831529e-06$	
L_∞	$1.34478935e-05$	$1.28655965e-05$	$1.23791217e-05$	$1.67203894e-05$	

Tables 16 and 17 report the numerical and exact solutions of the real and imaginary parts of Problem 2 for a fixed time step $\Delta t = 0.002$ at $\gamma = 0.5$, as the number of subintervals is increased through $N = 10, 20, 40, 80$. These tables examine the effect of spatial mesh refinement while the time

step is kept fixed, in the same manner as Tables 3 and 4 for Problem 1. For the real part, represented in Table 16, the nodal values are identical to the displayed precision for all values of N, and the error norms change only slightly as the spatial mesh is refined. In particular, the L_2 error changes from 7.0964×10^{-5} at $N = 10$ to approximately 7.0969×10^{-5} at $N = 80$. The imaginary part, in Table 17 exhibits similar behavior, with the error norms remaining of order 10^{-5} and showing very little change as N increases. Thus, for the fixed value $\Delta t = 0.002$ and the range of spatial meshes considered here, further spatial refinement produces negligible improvement in the total error. This indicates that the remaining error is predominantly associated with the temporal discretization for this experiment.

Table 16. Comparison of numerical and exact solutions for the real part of Problem 2 for $\Delta t = 0.002$, $t_f = 1$, $\gamma = 0.5$, and different values of N.

x	$N = 10$	$N = 20$	$N = 40$	$N = 80$	Exact solution
0.0	0.000000	0.000000	0.000000	0.000000	0.000000
0.1	0.089979	0.089979	0.089979	0.089979	0.090000
0.2	0.159958	0.159958	0.159958	0.159958	0.160000
0.3	0.209938	0.209938	0.209938	0.209938	0.210000
0.4	0.239920	0.239920	0.239920	0.239920	0.240000
0.5	0.249907	0.249907	0.249907	0.249907	0.250000
0.6	0.239900	0.239900	0.239900	0.239900	0.240000
0.7	0.209902	0.209902	0.209902	0.209902	0.210000
0.8	0.159917	0.159917	0.159917	0.159917	0.160000
0.9	0.089949	0.089949	0.089949	0.089949	0.090000
1.0	0.000000	0.000000	0.000000	0.000000	0.000000
L_2	7.09640475$e-05$	7.09683594$e-05$	7.09685031$e-05$	7.09685100$e-05$	
L_∞	1.00350249$e-04$	1.00559534$e-04$	1.00766982$e-04$	1.00767018$e-04$	

Table 17. Comparison of numerical and exact solutions for the imaginary part of Problem 2 for $\Delta t = 0.002$, $t_f = 1$, $\gamma = 0.5$, and different values of N.

x	$N = 10$	$N = 20$	$N = 40$	$N = 80$	Exact Solution
0.0	0.000000	0.000000	0.000000	0.000000	0.000000
0.1	0.010006	0.010006	0.010006	0.010006	0.010000
0.2	0.040011	0.040011	0.040011	0.040011	0.040000
0.3	0.090013	0.090013	0.090013	0.090013	0.090000
0.4	0.160011	0.160011	0.160011	0.160011	0.160000
0.5	0.250004	0.250004	0.250004	0.250004	0.250000
0.6	0.359995	0.359995	0.359995	0.359995	0.360000
0.7	0.489985	0.489985	0.489985	0.489985	0.490000
0.8	0.639977	0.639977	0.639977	0.639977	0.640000
0.9	0.809978	0.809978	0.809978	0.809978	0.810000
1.0	1.000000	1.000000	1.000000	1.000000	1.000000
L_2	1.32993767$e-05$	1.33429869$e-05$	1.33458990$e-05$	1.33460843$e-05$	
L_∞	2.34861803$e-05$	2.46636158$e-05$	2.46647867$e-05$	2.46648805$e-05$	

Table 18 compares the error norms obtained by the present method with those reported in [11] for Problem 2 at $\gamma = 0.1$, $N = 40$, and $t = 1$, as the time step is decreased from $\Delta t = 1/16$ to $1/32$ and $1/64$. For both the real and imaginary parts, the error norms obtained by the present method are smaller than the corresponding values reported in [11] for all three time steps considered. Moreover, the L_2 and L_∞ errors of the present method decrease steadily as Δt is refined. Thus, for this test problem and the parameter values considered in Table 18, the present high-order cubic B-spline approach yields smaller reported error norms than the trigonometric B-spline collocation results given in [11].

Table 18. Comparison of the error norms of the present method with those reported in [11] for the real and imaginary parts of Problem 2 with $\gamma = 0.1$, $N = 40$, $t = 1$, and different values of Δt.

Real part				
	Present method		[11]	
Δt	L_2	L_∞	L_2	L_∞
1/16	2.45632e-03	3.46400e-03	1.23434e-02	1.69582e-02
1/32	1.16784e-03	1.65277e-03	8.50622e-03	6.19172e-03
1/64	5.67004e-04	8.02306e-04	3.10742e-03	4.26873e-03

Imaginary part				
	Present method		[11]	
Δt	L_2	L_∞	L_2	L_∞
1/16	3.78018e-04	6.88825e-04	6.12270e-02	1.64917e-02
1/32	2.00864e-04	3.67089e-04	6.09586e-03	8.22627e-03
1/64	1.03808e-04	1.95912e-04	3.05180e-03	4.11967e-03

In Tables 19 and 20, the time step is selected according to the balanced refinement relation $\Delta t = Ch^4$ so that the first-order temporal consistency contribution $O(\Delta t)$ and the fourth-order spatial consistency contribution $O(h^4)$ are of the same formal order. Table 19 presents the results for the real part and Table 20 for the imaginary part of Problem 2, both with $\gamma = 0.8$.

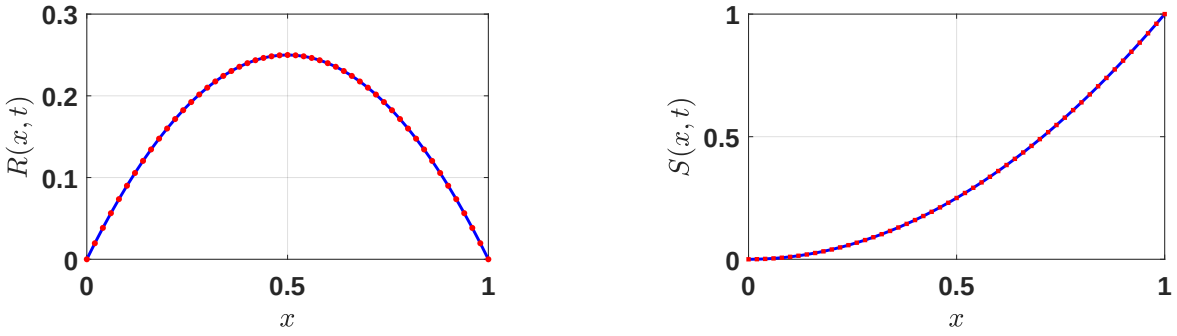
Table 19. Maximum absolute errors and convergence rates for the real part of Problem 2 under the joint-refinement strategy $\Delta t = Ch^4$ for different values of N.

N	Δt	L_∞	RoC
10	1/5	$8.0712261181e-03$	–
20	1/80	$6.1855939140e-04$	3.70
40	1/1280	$3.9568066488e-05$	3.96
80	1/20480	$2.4911359221e-06$	3.98

Table 20. Maximum absolute errors and convergence rates for the imaginary part of Problem 2 under the joint-refinement strategy $\Delta t = Ch^4$ for different values of N.

N	Δt	L_∞	RoC
10	1/5	$4.0670850468e-03$	–
20	1/80	$1.5052852104e-04$	4.75
40	1/1280	$9.6222712292e-06$	3.96
80	1/20480	$5.9815683551e-07$	4.00

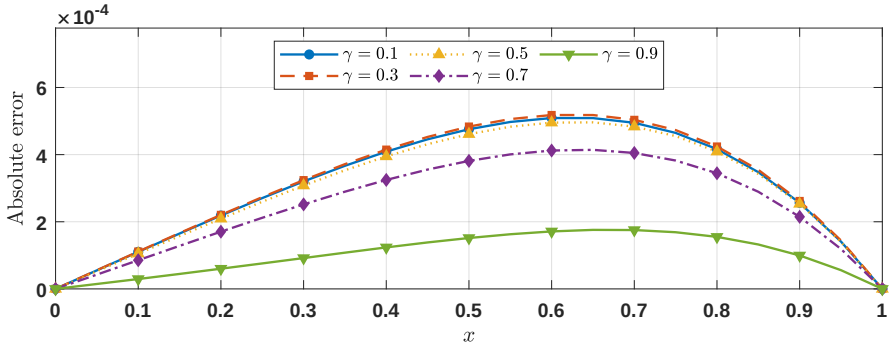
Under this joint-refinement strategy, the observed convergence rates approach four as the mesh is refined for both components. These results are consistent with the combined error behavior predicted by the local consistency analysis of Section 5. Figure 5 compares the numerical and exact solutions of the real and imaginary parts of Problem 2, obtained with $N = 50$, $\Delta t = 0.001$, and $\gamma = 0.5$ at $t_f = 1$. Consistent with the small error norms reported in the tables, the differences between the numerical and exact solutions are not visually distinguishable, and the corresponding curves nearly overlap for both the real and imaginary parts.



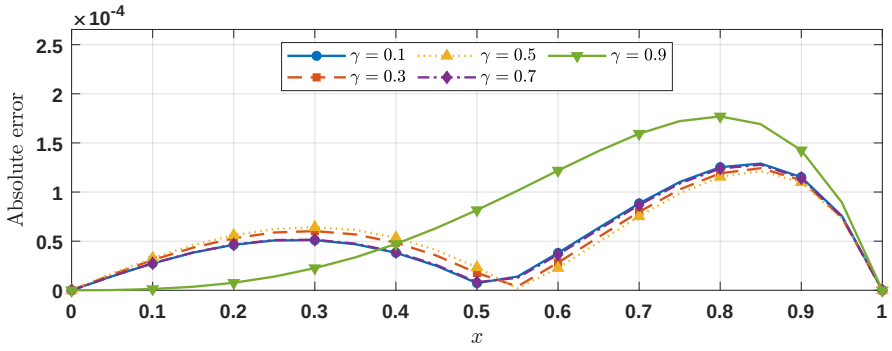
(a) Real part **(b)** Imaginary part

Figure 5. Comparison of the numerical solution (circles) and the exact solution (solid line) for the real and imaginary parts of Problem 2 for $N = 50$, $\Delta t = 0.001$, and $\gamma = 0.5$ at $t_f = 1$.

Figure 6a,6b presents the absolute error distributions for the real and imaginary parts of Problem 2 at $t = 1$ for $N = 20$; $\Delta t = 0.01$; and $\gamma = 0.1, 0.3, 0.5, 0.7, 0.9$. In both figures, the error vanishes at the two boundaries in accordance with the prescribed boundary conditions and develops in the interior of the domain. For the real part, the error exhibits a single smooth interior peak, with the curve corresponding to $\gamma = 0.9$ lying below the other curves over most of the interval. For the imaginary part, a different error pattern is observed. In particular, the error corresponding to $\gamma = 0.9$ is relatively small in the left part of the interval but increases substantially toward the right part and develops the largest peak near $x = 0.8$. Thus, for this test problem, the fractional order affects not only the magnitude but also the spatial distribution of the numerical error.



(a) Real part



(b) Imaginary part

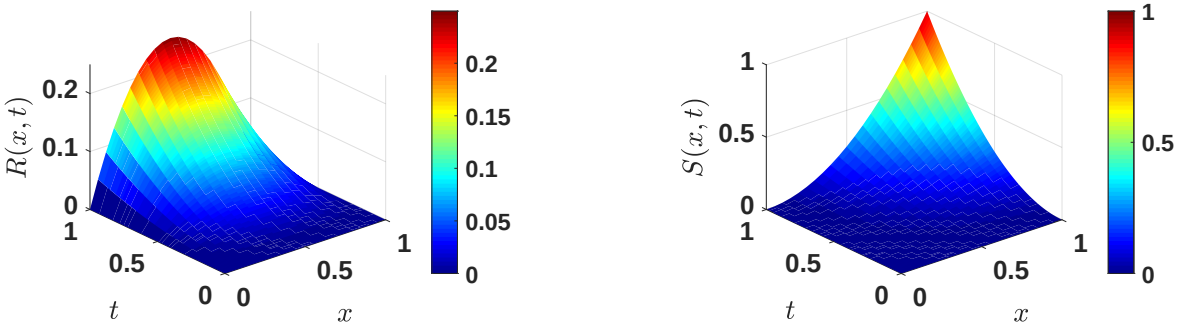
Figure 6. Distribution of the absolute error across the domain at $t = 1$ for the real part (top) and the imaginary part (bottom) of Problem 2 for $N = 20$; $\Delta t = 0.01$; and $\gamma = 0.1, 0.3, 0.5, 0.7, 0.9$.

Figure 7a,7b presents the numerical solution of Problem 2 as surfaces over the space–time plane for the real and imaginary parts, respectively, obtained with $N = 20$, $\Delta t = 0.01$, and $\gamma = 0.5$. Both surfaces start from the zero initial condition at $t = 0$ and gradually develop their spatial profiles as time increases. The real part develops an interior maximum and vanishes at both spatial boundaries, whereas the imaginary part increases with x and reaches its largest value at the boundary $x = 1$. The amplitudes of both components increase with time, in accordance with the t^2 dependence of the exact solution.

Figure 8 illustrates the L_∞ errors for the real and imaginary parts of Problem 2 under a joint spatial–temporal refinement, with $\gamma = 0.8$. In this experiment, halving the spatial step size is accompanied by a tenfold reduction in the time step, corresponding to

$$\Delta t \propto h^{\log_2(10)} \approx h^{3.322}.$$

This refinement relation differs from the balanced relation $\Delta t = Ch^4$ used in Tables 19 and 20, and Figure 8 is reported as a separate experiment. The error curves decrease rapidly under this joint refinement and are shown together with a reference line of slope four. Because both h and Δt vary simultaneously here, the slopes in this figure represent the combined influence of the temporal and spatial discretizations and should not be interpreted as a direct measurement of the spatial convergence order; this is consistent with the local consistency error $O(\Delta t + h^4)$ established in Section 5.



(a) Real part **(b)** Imaginary part

Figure 7. Space–time surfaces of the numerical solution for the real part (left) and the imaginary part (right) of Problem 2 for $N = 20$, $\Delta t = 0.01$, and $\gamma = 0.5$.

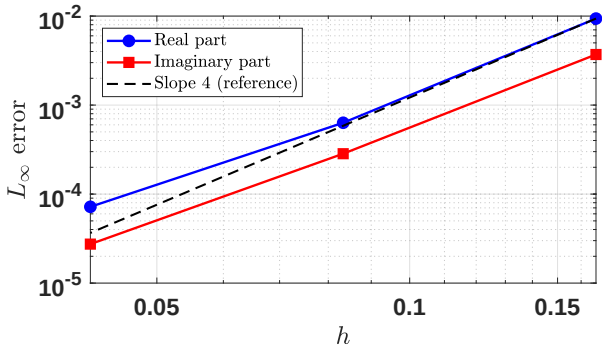


Figure 8. L_∞ error under a joint spatial–temporal refinement for the real and imaginary parts of Problem 2 at $\gamma = 0.8$, with $\Delta t \propto h^{\log_2(10)} \approx h^{3.322}$; this refinement relation differs from the balanced relation $\Delta t = Ch^4$ used in Table 19. The dashed reference line has slope four.

7.3. Problem 3

To further examine the performance of the proposed method in the presence of limited temporal regularity, we consider a nonsmooth test problem of Example 3 in [14]. The time-fractional nonlinear Schrödinger equation

$$i\frac{\partial^\gamma u}{\partial t^\gamma} + \frac{\partial^2 u}{\partial x^2} + |u|^2 u = f_3(x,t), \qquad 0 < x < 1, \quad 0 < t \le 1, \quad 0 < \gamma < 1 \tag{7.10}$$

is considered with the homogeneous boundary conditions

$$u(0,t) = u(1,t) = 0 \tag{7.11}$$

and the initial condition

$$u(x,0) = 0. \tag{7.12}$$

The exact solution is taken as

$$u(x,t) = \left(t^3 + t^\gamma\right)\sin(\pi x). \tag{7.13}$$

Accordingly, the corresponding source term is

$$f_3(x,t) = i\left(\frac{6t^{3-\gamma}}{\Gamma(4-\gamma)} + \Gamma(1+\gamma)\right)\sin(\pi x) - \pi^2\left(t^3 + t^\gamma\right)\sin(\pi x) + \left[\left(t^3 + t^\gamma\right)\sin(\pi x)\right]^3. \tag{7.14}$$

Unlike the smooth test problems considered above, the solution (7.13) has limited temporal regularity near the initial time. Indeed,

$$u_t(x,t) = \left(3t^2 + \gamma t^{\gamma-1}\right)\sin(\pi x), \tag{7.15}$$

and therefore $u_t(x,t)$ becomes unbounded as $t \to 0^+$ for $0 < \gamma < 1$. Thus, this example contains the weak initial singularity that commonly arises in time-fractional evolution problems. In particular, the smoothness assumptions employed in the local consistency analysis of Section 5 are not satisfied by this test solution at $t = 0$. The numerical experiment is performed with $\gamma = 0.5$, $t_f = 1$, and $N = 80$. The spatial mesh is kept fixed while the time step is successively halved from $\Delta t = 1/50$ to $\Delta t = 1/800$. The resulting errors and observed temporal rates are reported in Table 21. The rates are calculated using

$$\text{Rate} = \frac{\log(E_{\Delta t}/E_{\Delta t/2})}{\log 2}.$$

Table 21. Temporal refinement results for the nonsmooth solution of Problem 3 with $\gamma = 0.5$, $N = 80$, and $t_f = 1$.

Δt	$L_2(u)$	Rate	$L_\infty(u)$	Rate
1/50	4.5794881×10^{-2}	–	6.7406530×10^{-2}	–
1/100	2.6173443×10^{-2}	0.807	3.8532500×10^{-2}	0.807
1/200	1.4225035×10^{-2}	0.880	2.0944295×10^{-2}	0.880
1/400	7.4643788×10^{-3}	0.930	1.0990823×10^{-2}	0.930
1/800	3.8322120×10^{-3}	0.962	5.6428543×10^{-3}	0.962

Table 21 shows a systematic decrease in both error norms as the time step is refined. The observed rates increase from approximately 0.81 on the coarser temporal meshes to approximately 0.96 on the finest pair of meshes. Thus, although the exact solution possesses a weak initial singularity and does not satisfy the temporal smoothness assumptions used in Section 5, the present computation exhibits an approximately first-order temporal behavior as the time step is refined. To verify that the behavior observed in Table 21 is not dominated by the spatial discretization, an additional spatial-mesh check was carried out at the smallest time step $\Delta t = 1/800$. The $L_\infty(u)$ errors obtained with $N = 40$, 80, and 160 were 5.6437562×10^{-3}, 5.6428543×10^{-3}, and 5.6427978×10^{-3}, respectively. The corresponding $L_2(u)$ errors were 3.8328312×10^{-3}, 3.8322120×10^{-3}, and 3.8321732×10^{-3}. The negligible variation under this spatial refinement indicates that for the parameters used in Table 21, the reported error behavior is predominantly associated with the temporal discretization. Moreover, the differences between the errors obtained with $N = 40$, 80 and 160 decrease by a factor of approximately 16, which is consistent with an $O(h^4)$ spatial contribution added to a temporal error that does not depend on N. It is important to emphasize that the results of this nonsmooth test are numerical observations rather than a convergence theorem for solutions with initial singularities. Nevertheless, the experiment

demonstrates that the proposed scheme remains effective for this weakly singular test problem and complements the smooth-solution experiments presented in the preceding subsections.

8. Conclusions

In this paper, a numerical method is presented for the time-fractional nonlinear Schrödinger equation with the Caputo fractional derivative. The time derivative is discretized by the L1 algorithm together with Crank–Nicolson-type averaging, and the nonlinear coefficient is evaluated explicitly at the previous time level. The space discretization is carried out by a collocation method based on cubic B-spline functions. The second-order spatial derivative is approximated by a high-order approach in order to increase the spatial accuracy of the scheme. A local consistency analysis for sufficiently smooth solutions shows that the complete discretization has local truncation error $O(\Delta t + h^4)$. Thus, the complete temporal discretization is first-order consistent, whereas the high-order spatial approximation is fourth-order accurate. The separate temporal and spatial refinement studies are consistent with these respective behaviors. Cubic; trigonometric; and uniform hyperbolic polynomial B-spline bases are also examined numerically. Although these basis functions can be written in a common algebraic form, the fourth-order spatial analysis developed in this study is associated with the corrected cubic B-spline approximation and is not automatically transferred to the other B-spline families. The stability-related behavior of the corresponding linearized frozen-coefficient recurrence is investigated through Fourier resolvent analysis. For the fractional case, the L1 memory term leads to a convolution recurrence rather than a single time-independent amplification factor. The resulting resolvent denominator is shown to have no zeros in the open unit disk under the stated assumptions. This pole-free property is not interpreted as a proof of unconditional stability in the stronger sense of a uniform bound on all time-level Fourier coefficients. The scheme is applied to three test problems, and its accuracy is measured through the L_2 and L_∞ error norms, observed rates of convergence, and comparisons with results reported in the literature. For the smooth test problems, the numerical experiments exhibit approximately first-order temporal behavior; for Problem 1, they exhibit approximately fourth-order spatial behavior, when temporal and spatial refinements are examined separately. In addition, a nonsmooth test problem with a weak initial singularity is considered. For this problem, the errors decrease systematically under temporal refinement, with the observed rates approaching first-order behavior on the finer temporal meshes, despite the limited temporal regularity of the exact solution. The results indicate that the proposed high-order B-spline collocation method provides accurate numerical approximations for the considered time-fractional nonlinear Schrödinger test problems.

Author contributions

A.E.: Methodology, Validation, Conceptualization, Formal Analysis, Investigation, Visualization. M.Ö.: Resources, Validation, Conceptualization, Investigation, Visualization. B.K.: Writing – Original Draft, Methodology, Validation, Conceptualization, Formal Analysis, Investigation, Visualization. All authors have read and approved the final version of the manuscript for publication.

Use of Generative-AI tools declaration

The authors declare that they have used Artificial Intelligence (AI) tools for language editing and proofreading purposes.

Acknowledgments

This work was supported by the Research Fund of Inonu University via project number FBA-2026-4241.

Conflict of interest

The authors declare that they have no known competing financial interests or personal relationships that could have appeared to influence the work reported in this paper. The authors declare no conflict of interest.

References

1. B. N. Narahari Achar, B. T. Yale, J. W. Hanneken, Time fractional Schrödinger equation revisited, *Adv. Math. Phys.*, **2013** (2013), 290216. https://doi.org/10.1155/2013/290216
2. C. Sulem, P. L. Sulem, *The nonlinear Schrödinger equation: self-focusing and wave collapse*, Applied Mathematical Sciences, Vol. 139, New York: Springer, 1999. https://doi.org/10.1007/b98958
3. A. Amer, E. K. Jaradat, H. U. Rehman, Y. Yildirim, S. Abu Alrub, M. S. Ateto, Exact and numerical optical soliton solutions of the fractional quadratic–cubic nonlinear Schrödinger equation in conformable derivative framework, *Sci. Rep.*, **16** (2026), 15118. https://doi.org/10.1038/s41598-026-43272-7
4. M. A. Mustafa, M. A. S. Murad, Soliton solutions for time-fractional (3+1)-dimensional nonlinear Schrödinger equation with cubic-quintic nonlinearity terms, *Int. J. Comput. Math.*, **102** (2025), 1428–1442. https://doi.org/10.1080/00207160.2025.2499879
5. S. Panwar, R. M. Pandey, P. Rai, An analysis of the nonlinear time-fractional Schrödinger and coupled Klein–Gordon–Schrödinger equations, *New Math. Nat. Comput.*, 2026, 1–21. https://doi.org/10.1142/S1793005728500172
6. A. Hagag, Z. Alqahtani, A. Arafa, Efficient analytic technique for fractional fourth-order cubic nonlinear Schrödinger equation, *Rev. Int. Métodos Numér. Cálc. Diseño Ing.*, **41** (2025), 16. https://doi.org/10.23967/j.rimni.2024.10.60138
7. A. A. M. Arafa, A. M. S. Hagag, Q-homotopy analysis transform method applied to fractional Kundu–Eckhaus equation and fractional massive Thirring model arising in quantum field theory, *Asian-Eur. J. Math.*, **12** (2019), 1950045. https://doi.org/10.1142/S1793557119500451
8. D. Shi, Z. Li, Neural network-driven exact solutions for the conformal nonlinear fractional Kolmogorov–Petrovskii–Piskunov model, *Phys. Lett. A*, **593** (2026), 132023. https://doi.org/10.1016/j.physleta.2026.132023

9. H. Lv, Exact traveling wave solutions of the paraxial wave equation with conformable fractional derivative using an enhanced direct algebraic method, *Symmetry*, **18** (2026), 1300. https://doi.org/10.3390/sym18081300
10. A. Mohebbi, M. Abbaszadeh, M. Dehghan, The use of a meshless technique based on collocation and radial basis functions for solving the time fractional nonlinear Schrödinger equation arising in quantum mechanics, *Eng. Anal. Boundary Elem.*, **37** (2013), 475–485. https://doi.org/10.1016/j.enganabound.2012.12.002
11. A. R. Hadhoud, A. A. M. Rageh, T. Radwan, Computational solution of the time-fractional Schrödinger equation by using trigonometric B-spline collocation method, *Fractal Fract.*, **6** (2022), 127. https://doi.org/10.3390/fractalfract6030127
12. M. A. Bayrak, A. Demir, Numerical solution of space fractional Schrödinger equation by fractional Clique collocation method, *Kafkas Üniv. Fen Bilimleri Enst. Derg.*, **18** (2025), 54–59. https://doi.org/10.58688/kujs.1702711
13. S. Nemati, S. Sedaghat, S. Arefi, A new numerical approach for solving space–time fractional Schrödinger differential equations via fractional-order Chelyshkov functions, *Results Appl. Math.*, **26** (2025), 100584. https://doi.org/10.1016/j.rinam.2025.100584
14. Y. Wang, B. Yin, Y. Liu, H. Li, Modified L1 Crank–Nicolson finite element methods with unconditional convergence for nonlinear time-fractional Schrödinger equations, *Commun. Nonlinear Sci. Numer. Simul.*, **143** (2025), 108623. https://doi.org/10.1016/j.cnsns.2025.108623
15. X. Zhou, M. Zhang, C. Liao, Unconditionally stable L1-2 FEMs for nonlinear Schrödinger equations with the variable-order time-fractional derivative, *Mathematics*, **14** (2026), 1656. https://doi.org/10.3390/math14101656
16. M. Serik, R. Eskar, P. Huang, Numerical solution of time-fractional Schrödinger equation by using FDM, *Axioms*, **12** (2023), 816. https://doi.org/10.3390/axioms12090816
17. A. M. Hayat, M. Abbas, H. Emadifar, A. S. M. Alzaidi, T. Nazir, F. A. Abdullah, An efficient computational scheme for solving coupled time-fractional Schrödinger equation via cubic B-spline functions, *PLoS ONE*, **19** (2024), e0296909. https://doi.org/10.1371/journal.pone.0296909
18. M. Önal, B. Karaağaç, A. Esen, An efficient higher-order trigonometric cubic B-spline collocation method for time-fractional Burgers equations, *Int. J. Math. Comput. Eng.*, **4** (2026), 211–234. https://doi.org/10.2478/ijmce-2026-0013
19. C. Li, W. Deng, Remarks on fractional derivatives, *Appl. Math. Comput.*, **187** (2007), 777–784. https://doi.org/10.1016/j.amc.2006.08.163
20. Y. Lin, C. Xu, Finite difference/spectral approximations for the time-fractional diffusion equation, *J. Comput. Phys.*, **225** (2007), 1533–1552. https://doi.org/10.1016/j.jcp.2007.02.001
21. H. Zhang, F. Liu, M. S. Phanikumar, M. M. Meerschaert, A novel numerical method for the time variable fractional order mobile–immobile advection–dispersion model, *Comput. Math. Appl.*, **66** (2013), 693–701. https://doi.org/10.1016/j.camwa.2013.01.031
22. A. R. Khlefha, A comprehensive review of applications of spline function, *Int. Acad. J. Sci. Eng.*, **11** (2024), 322–331. https://doi.org/10.9756/iajse/v11i1/iajse1138

23. V. Dahiya, Exploring B-spline functions for numerical solution of mathematical problems, *Int. J. Multidiscip. Res. Dev.*, **2** (2015), 452–458.

24. G. Walz, Identities for trigonometric B-splines with an application to curve design, *BIT Numer. Math.*, **37** (1997), 189–201. https://doi.org/10.1007/BF02510180

25. M. S. Palav, V. H. Pradhan, Redefined fourth order uniform hyperbolic polynomial B-splines based collocation method for solving advection–diffusion equation, *Appl. Math. Comput.*, **484** (2025), 128992. https://doi.org/10.1016/j.amc.2024.128992

26. T. R. Lucas, Error bounds for interpolating cubic splines under various end conditions, *SIAM J. Numer. Anal.*, **11** (1974), 569–584. https://doi.org/10.1137/0711049

27. R. C. Mittal, R. Rohila, A fourth order cubic B-spline collocation method for the numerical study of the RLW and MRLW equations, *Wave Motion*, **80** (2018), 47–68. https://doi.org/10.1016/j.wavemoti.2018.04.001

28. R. Rohila, R. C. Mittal, Numerical study of reaction diffusion Fisher's equation by fourth order cubic B-spline collocation method, *Math. Sci.*, **12** (2018), 79–89. https://doi.org/10.1007/s40096-018-0247-3

29. O. Taşbozan, *Kesirli mertebeden kısmi diferansiyel denklemlerin B-spline sonlu eleman yöntemleri ile Çözümleri [Solutions of fractional order partial differential equations by B-spline finite element methods]*, PhD thesis, Turkey: İnönü University, 2015.



AIMS Press

© 2026 the Author(s), licensee AIMS Press. This is an open access article distributed under the terms of the Creative Commons Attribution License (http://creativecommons.org/licenses/by/4.0)